Department of Physics and Astronomy
University of Heidelberg

Master Thesis

in Physics

submitted by

Max Hilaire Wolter

born in Luxembourg

2014

Two-pulse dielectric polarisation echo experiments on the multicomponent glasses BK7 and HY-1

This Master thesis has been carried out by Max H. Wolter

at the

Kirchhoff-Institute for Physics

under the supervision of

Prof. Dr. C. Enss

The low temperature properties of glasses are dominated by atomic tunnelling systems (TSs) which can be described by the phenomenological standard tunnelling model. This model is successful in describing many of the physical properties but does not account for interactions between TSs, in particular the interaction between neighbouring TSs via phase decoherence caused by spectral diffusion, and possible nuclear effects. Two-pulse dielectric polarisation echo experiments represent an appropriate technique to investigate the relaxation and decoherence processes of TSs in glasses. In the framework of this thesis, the decay of the echo amplitude in the borosilicate glass BK7 was measured for the first time inside a nuclear demagnetisation refrigerator at temperatures down to 2.1 mK. The decay curves measured below 4 mK exhibited a peculiar bump that may hint at a possible phase transition of the glass. Further echo measurements were conducted on the multicomponent glass HY-1, containing a noticeable amount of holmium which carries a very large nuclear electric quadrupole moment, with and without application of a magnetic field. They have revealed additional relaxation and decoherence processes that may be partly due to nuclear effects and due to the magnetic properties of the glass.

Dielektrische Zweipuls-Echomessungen
an den Multikomponentengläsern BK7 und HY-1

Die Tieftemperatureigenschaften von Gläsern werden von atomaren Tunnelsystemen, welche durch das phänomenologische Standardtunnelmodell beschrieben werden können, bestimmt. Durch dieses Modell können viele physikalische Eigenschaften erfolgreich beschrieben werden. Jedoch ist das Modell nicht in der Lage die Wechselwirkung zwischen Tunnelsystemen, insbesondere die durch spektrale Diffusion hervorgerufene Phasendekohärenz, sowie eventuelle durch Kerne hervorgerufene Effekte, zu beschreiben. Mittels dielektrischen Zweipuls-Echomessungen ist es möglich die Relaxations- und Dekohärenzprozesse von Tunnelsystemen in Gläsern zu untersuchen. Im Rahmen dieser Arbeit wurde erstmalig der Zerfall der Echoamplitude des Borosilikatglases BK7 in einem Kernentmagnetisierungskryostaten bis zu Temperaturen von 2.1 mK gemessen. Dabei wurde eine Beule, welche auf einen möglichen Phasenübergang hinweist, in den Echozerfallskurven unter 4 mK festgestellt. Weitere Echomessungen wurden im Nullfeld und im Magnetfeld an dem Multikomponentenglas HY-1 durchgeführt. Dieses Glas enthält einen merklichen Anteil von Holmium welches sich durch ein großes elektrischen Kernquadrupolmoment auszeichnet. Die Messungen weisen auf zusätzliche Relaxations- und Dekohärenzprozesse hin, welche teils durch Kerneffekte, teils durch magnetische Eigenschaften des Glases hervorgerufen werden könnten.

Contents

1. Introduction

One of the most interesting research areas investigating both fundamental questions and technological advancement is condensed matter physics, a branch of physics that deals with the physical properties of solids.

Solids can be categorised into two groups: crystals and amorphous solids or glasses. The atoms or molecules that make up the crystals are situated at well-defined positions in a periodically-repeating lattice structure, leading to short and long range order and can thus be very accurately described by theory. Amorphous solids do not exhibit such an organised structure but have their constituents situated randomly which results in short range but not in long range order.

Dielectric glasses are a typical example of amorphous solids and are formed by rapidly cooling down a melt. The glass transition occurs once the viscosity surpasses the value of 10^{13} Poise, meaning that the melt has frozen and henceforth exists as a disordered, solid structure. In contrast to crystalline solids, the glassy structure does not exhibit a long range order. This inherent disorder leads to fundamental differences in the properties of glasses compared to crystals.

At very low temperatures, dielectric glasses present substantial differences in their thermal, acoustic and dielectric properties from those observed in their crystalline counterparts [Zel71]. In particular, the thermal conductivity of a wide array of different glass types was shown to be very similar both qualitatively and quantitatively, independent of the chemical composition of the glasses [Poh02]. It was thus reasoned that the particular properties of glasses are due to their structural disorder, irrespective of the atomic properties of their constituents. As a physical interpretation, low-energy excitations of single atoms or groups of atoms were advocated and phenomenologically described as tunnelling systems in the so-called standard tunnelling model introduced in 1972 [And72] [Phi72]. This model is based on the assumption that the low-energy excitations can occupy two energetically favourable positions separated by a potential barrier. At very low temperatures, they lack the required thermal energy to overcome this barrier but are still able to change their equilibrium position via quantum tunnelling.

Although the standard tunnelling model is very successful in describing a variety of thermal, acoustic and dielectric properties in glasses [Phi81], it also presents some deficiencies. On one hand, it fails to deliver a microscopic picture of the tunnelling systems and on the other hand it neglects interactions between tunnelling systems. In fact, it has since been shown that tunnelling systems are able to interact with their environment via the exchange of thermal phonons. Additionally, they are also able to mutually interact with one another

which can be decribed by the theory of spectral diffusion [KA62] [BH77] [Hu74]. Both types of interaction lead to relaxation mechanisms that can be experimentally investigated via dielectric polarisation echoes.

In the framework of this thesis, two-pulse polarisation echo experiments were conducted. The echoes were produced by exciting a glass sample via two brief, high-frequency electric field pulses. These cause a macroscopic dielectric polarisation, or echo, to form as a result of the coherent behaviour of the resonant tunnelling systems at sufficiently low temperatures. By increasing the pulse separation or temperature, the resonantly excited tunnelling systems are subject to increasing phase decoherence effects due to relaxation mechanisms which ultimately leads to a smaller macroscopic polarisation.

Different polarisation echo experiments conducted on the dielectric multicomponent glasses BK7 [Fas10] [Sch10] [Sch12] [Fic13] and AlBaSi [Arc13] [Ahr13] have already extensively investigated the relaxation mechanisms in a temperature range between $7\,\mathrm{mK}$ and $70\,\mathrm{mK}$. Previous dielectric constant experiments carried out on the AlBaSi glass have provided evidence for a possible phase transition below a critical temperature of $T_\mathrm{c} = 5.84\,\mathrm{mK}$ [Str98]. It is assumed that the uncorrelated and incoherent tunnelling motion of the individual tunnelling systems at higher temperatures is crossing over into a coherent and collective tunnelling motion below T_c. The same behaviour was also observed in other multicomponent glasses such as BK7, which is a well-known glass since its acoustic and dielectric properties have already extensively been investigated [Hun76] [Woh01]. Thus the principal aim of this project is to study the interactions of the tunnelling systems in BK7 below the critical temperature by measuring two-pulse polarisation echoes for the first time inside a nuclear demagnetisation refrigerator able to generate temperatures in the microkelvin regime.

In addition to the already mentioned relaxation mechanisms, it is assumed that nuclear effects could also be leading to a phase decoherence of the tunnelling systems in glasses [Wue02] [Wue04]. More specifically, the electric quadrupole moments of the nuclei can interact with local electric field gradients leading to a hyperfine splitting of the two original energy levels considered in the standard tunnelling model which ultimately results in additional destructive interference effects. This has already been shown in echo experiments on amorphous deuterated glycerol [Nag04] [Baz08]. In order to investigate this effect in multicomponent glasses, HY-1, containing a noticeable amount of holmium which carries a very large nuclear electric quadrupole moment, has been studied via two-pulse polarisation echoes with and without application of a magnetic field.

In chapter 2 the necessary theoretical background is laid out by beginning with a brief overview of the low temperature properties of glasses. Then the standard tunnelling model is introduced before the dielectric two-pulse polarisation echoes are theoretically explained.

Afterwards the interaction of the tunnelling systems with their environment and among one another are described. The chapter is concluded by a brief overview of nuclear effects. In chapter 3 the experimental setup used in the framework of this thesis is described by first providing an overview of the thermometers and sample holders used in the experiments. Then the integration of the latter into the cryostats is visualised before the electronic setup used for the measurement of the polarisation echoes is described. The chapter is concluded by an overview of the two glass samples that were investigated.

Chapter 4 starts by providing an analysis of the data evaluation of the measured quantities. Then the experimental results are presented and subsequently discussed.

The final chapter consists of a conclusion and a brief outlook of possible further experiments.

2. Theoretical background

In the first section of this chapter the anomalous behaviour of glasses compared to crystals at low temperatures is presented. Then the standard tunnelling model, most successful at describing the thermal, acoustic and dielectric properties of glasses at low temperatures, is introduced. This is followed by the theoretical description of two-pulse polarisation echoes before the chapter is concluded by an overview of possible interactions, which are not included in the standard tunnelling model, in glasses such as relaxation processes and nuclear effects.

2.1 Low temperature properties of glasses

At very low temperatures, i.e. below $1\,\mathrm{K}$, the thermal properties of dielectric glasses are dominated by phonons which possess wavelengths of the order of $1000\,\text{\AA}$ [Hun77]. These wavelengths are much larger than the interatomic distance which means that the glasses can be described, as is the case for crystals, in terms of an elastic continuum. Hence Debye's theory for the crystalline specific heat and thermal conductivity should be applicable to glasses in this temperature range. Experimental results, however, show that this is not the case. The specific heat of amorphous quartz as well as the theoretical temperature
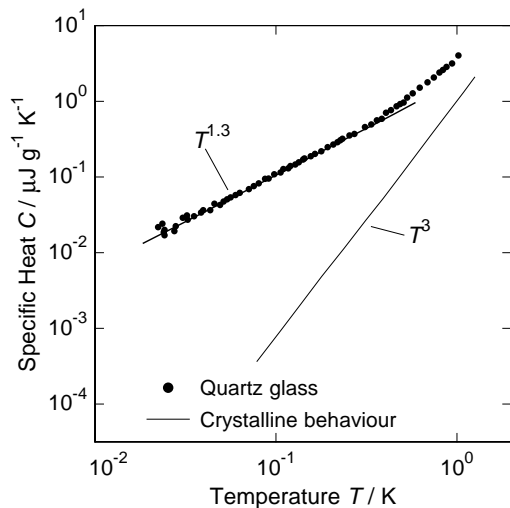
Figure 2.1: Comparison of the specific heat of quartz glass and quartz crystal as functions of temperature [Hun77]. Data taken from [Zel71] and [Las75].
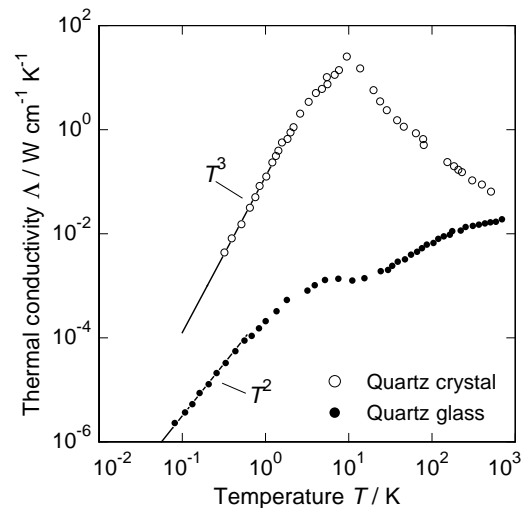
Figure 2.2: Comparison of the thermal conductivity of quartz glass and quartz crystal as functions of temperature [Zel71].

5

dependence of crystalline quartz are shown in Figure 2.1. While the Debye Model predicts the T^3-dependence of the specific heat of the crystal, the specific heat of amorphous SiO_2 is roughly linear for temperatures below 500 mK. Moreover, its absolute value is several orders of magnitude larger in the glassy state than in the crystalline state.

In contrast to the specific heat, Figure 2.2 shows that the thermal conductivity is substantially lower for amorphous quartz than for crystalline quartz. While the kinetic gas theory and the Debye Model can explain the T^3-dependence of the thermal conductivity of quartz crystal at very low temperatures, the same theoretical approach is not able to predict the measured T^2-dependence of quartz glass [Zel71] [Poh02].

Further measurements of the thermal conductivity on a wide array of glass types have shown a very interesting peculiarity. In Figure 2.3 the thermal conductivities of completely different types of glasses such as the plastic PMMA, the molecular glass $CaKNO_3$ or the superconducting metallic glass ZrPd, are plotted against temperature. Even though these glass types all differ greatly in their chemical composition, their thermal conductivities show a nearly identical temperature dependence. Additionally, as indicated by the blue lines and double arrow, below 1 K, the absolute value of the thermal conductivity is, within one order of magnitude, comparable between the different materials. This quasi-independence of the chemical composition of glasses is known as the universality of glasses [Poh02].

The particular behaviour of glasses presented above can be explained by the presence of additional low-energy excitations with a wide energy distribution. On one hand these low-energy excitations can store energy and directly contribute to the specific heat, while on the other hand they are localised and thus able to act as scattering centers to reduce
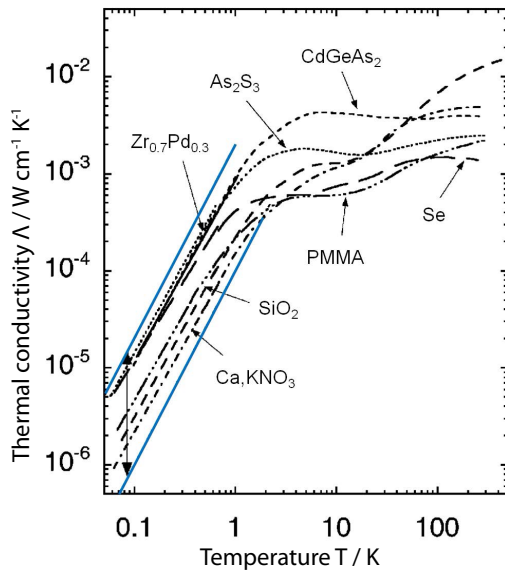
Figure 2.3: Thermal conductivity of a variety of glass types at low temperatures [Poh02]. The blue lines and the double arrow indicate the area within which all the absolute values lie.

the thermal conductivity at low temperatures. Furthermore, the universality of glasses implies that the low-energy excitations are not caused by the properties of the atoms or molecules that make up the glass but have their origin mainly in defects associated with the amorphous structure of the glass.

The nature of the aforementioned excitations and a phenomenological description are provided by the standard tunnelling model.

2.2 Standard tunnelling model

2.2.1 Double-well potential

In amorphous solids, single atoms or groups of atoms have no defined equilibrium positions and can move from one position to another leading to structural changes. This is represented schematically in Figure 2.4.

In 1972, the standard tunnelling model was introduced independently of each other by Phillips [Phi72] and Anderson et al. [And72]. This model identifies single atoms or groups of atoms as the aforementioned localised low-energy excitations in amorphous solids. These low-energy excitations can occupy several energetically favourable positions, colored yellow and orange in Figure 2.4, with slightly different energies and separated by a potential barrier.

At high temperatures, the atoms or groups of atoms are able to overcome the potential barrier via thermal hopping. At low temperatures, they lack the thermal energy necessary to jump across the potential barrier yet are still able to change their equilibrium position by tunnelling quantum mechanically between the potential minima.

To describe this tunnelling motion, the standard tunnelling model assumes a double-well potential as shown in Figure 2.5. In this picture, the low-energy excitations are represented by an effective particle of mass m sitting in either of the two wells separated by the
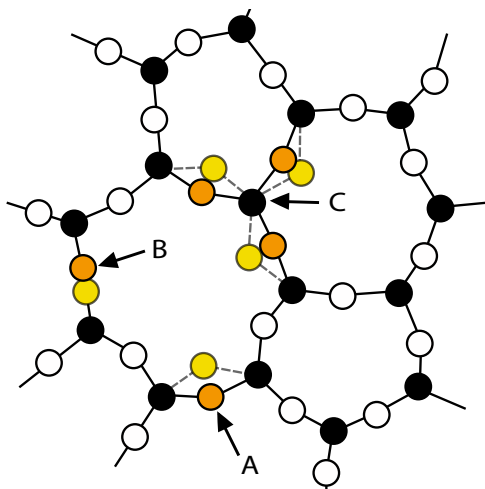
Figure 2.4: Two-dimensional structural representation of an amorphous solid. Single atoms or groups of atoms which have two equilibrium positions are labelled by A, B and C [Zac32] [Hun14].

potential barrier of height V and the distance d in configuration space. This configuration space is accounting for the fact that the two potential minima may not only distinguish themselves through physical separation but also through the orientation of the tunnelling atoms in the amorphous structure. The two wells are described by identical harmonic potentials with zero-point energy $\frac{1}{2}(\hbar\Omega \pm \Delta)$ and are shifted with respect to each other by the asymmetry energy Δ which characterises the difference in depth of the potentials and is due to the structural disorder of the glass. The normalised wavefunctions of the particle in the isolated left and right wells are denoted by ψ_{a} and ψ_{b} respectively.
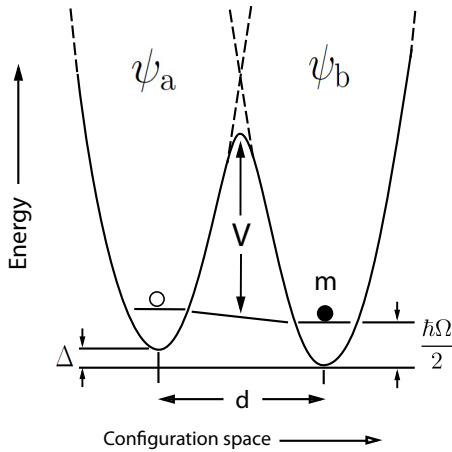
Figure 2.5: Schematic representation of a tunnelling particle of mass m in a double-well potential, characterising the tunnelling system.

At low temperatures, only the ground states of the potential wells are of interest. The double-well potential ensures a finite overlap of the particle wavefunctions in the isolated wells which results in a tunnelling process. Consequently, the total wavefunction of the particle in the double-well potential can be described by the linear superposition

$$\Psi = c_1\,\psi_{\mathrm{a}} + c_2\,\psi_{\mathrm{b}} \tag{2.1}$$

of the wavefunctions of the individual ground states. The coefficients c_1 and c_2 are assumed to be real quantities. The energy eigenvalue E of the system can be determined by solving the Schrödinger equation $H\Psi = E\Psi$ via the Rayleigh-Ritz variational method

$$E = \frac{\int \Psi^* H \Psi \, \mathrm{d}^3 x}{\int \Psi^* \Psi \, \mathrm{d}^3 x} = \frac{c_1^2 H_{\mathrm{aa}} + c_2^2 H_{\mathrm{bb}} + 2 c_1 c_2 H_{\mathrm{ab}}}{c_1^2 + c_2^2 + 2 c_1 c_2 S} \tag{2.2}$$

where the abbreviations $H_{\mathrm{aa}} = \int \psi_{\mathrm{a}}^* H \psi_{\mathrm{a}} \, \mathrm{d}^3 x$, $H_{\mathrm{bb}} = \int \psi_{\mathrm{b}}^* H \psi_{\mathrm{b}} \, \mathrm{d}^3 x$, $H_{\mathrm{ab}} = \int \psi_{\mathrm{a}}^* H \psi_{\mathrm{b}} \, \mathrm{d}^3 x$ and $S = \int \psi_{\mathrm{a}}^* \psi_{\mathrm{b}} \, \mathrm{d}^3 x$ have been used. Here H_{aa} and H_{bb} describe the eigenvalues of the particle in the isolated wells a and b respectively, $H_{\mathrm{ab}} = H_{\mathrm{ba}}$ denotes the exchange energy of the symmetric double-well potential and S represents the overlap of the wavefunctions.

The Rayleigh-Ritz variational method effectively retains the wavefunctions ψ_{a} and ψ_{b} and varies the coefficients c_1 and c_2 until a minimal eigenvalue E is found. This can be

expressed by $\partial E/\partial c_1 = 0$ and $\partial E/\partial c_2 = 0$. The results are the following secular equations

$$c_1(H_{\mathrm{aa}} - E) + c_2(H_{\mathrm{ab}} - ES) = 0 \tag{2.3}$$
$$c_1(H_{\mathrm{ab}} - ES) + c_2(H_{\mathrm{bb}} - E) = 0. \tag{2.4}$$

This is a set of simultaneous equations for the coefficients c_1 and c_2. For the solutions to exist, the secular determinant is required to be zero

$$(H_{\mathrm{aa}} - E)(H_{\mathrm{bb}} - E) - (H_{\mathrm{ab}} - ES)^2 = 0. \tag{2.5}$$

If the middle of the two potential minima is chosen as zero energy, the eigenvalues of the particle in the isolated wells can be written as $H_{\mathrm{aa}} = (\hbar\Omega + \Delta)/2$ and $H_{\mathrm{bb}} = (\hbar\Omega - \Delta)/2$ respectively. Additionally, the overlap of the wavefunctions is assumed to be negligible i.e. $S \approx 0$. As a result, the eigenvalues are given by

$$E_{\pm} = \frac{1}{2}\left(\hbar\Omega \pm \sqrt{\Delta^2 + 4H_{\mathrm{ab}}^2}\right) \tag{2.6}$$

with the splitting of the ground state

$$E = E_+ - E_- = \sqrt{\Delta^2 + 4H_{\mathrm{ab}}^2} = \sqrt{\Delta^2 + \Delta_0^2} \tag{2.7}$$

where Δ_0 denotes the tunnel splitting and is a measure of the tunnelling probability. For symmetric potentials, i.e. $\Delta = 0$, the energy splitting is just given by the tunnel splitting and the particle is with equal probability localised in either well. With increasing asymmetry energy Δ, the particle becomes more and more localised in a specific well.

With the aid of the WKB method it is possible to show that $\Delta_0 = -2H_{\mathrm{ab}} \approx \hbar\Omega\,\mathrm{e}^{-\lambda}$ with λ being the tunnelling parameter determined by the shape of the potential barrier and the mass m of the tunnelling particle. In the simple case described above, the tunnelling parameter can be approximated by

$$\lambda \approx \frac{d}{2\hbar}\sqrt{2mV}. \tag{2.8}$$

The two eigenvalues found in (2.6) imply that the tunnelling system can effectively be identified as a two-level system with energy splitting E. In the basis of the isolated potential wells $(\psi_{\mathrm{a}}, \psi_{\mathrm{b}})$, the tunnelling system is described by the Hamiltonian

$$H_0 = \frac{1}{2}\begin{pmatrix} \Delta & -\Delta_0 \\ -\Delta_0 & -\Delta \end{pmatrix} \tag{2.9}$$

where the constants $\hbar\Omega$ have been omitted. However (2.9) does not describe the eigenstates of the two-level system because it does not account for the tunnelling process. By making use of the total wavefunction of the particle in the double-well potential (2.1) and the eigenvalues (2.6), it is possible to construct the eigenfunctions of the two-level system

$$\Psi_+ = \psi_{\mathrm{a}}\cos\phi + \psi_{\mathrm{b}}\sin\phi \tag{2.10a}$$
$$\Psi_- = -\psi_{\mathrm{a}}\sin\phi + \psi_{\mathrm{b}}\cos\phi \tag{2.10b}$$

with $\tan(2\phi) = \Delta_0/\Delta$. As is portrayed in Figure 2.6, the symmetric wavefunction Ψ_+ characterises the ground state while the antisymmetric wavefunction Ψ_- characterises the excited state of the tunnelling system.
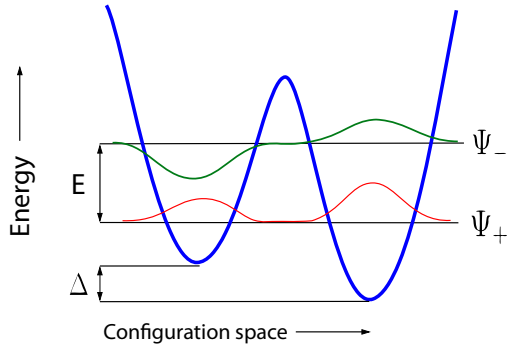
Figure 2.6: The symmetric ground state Ψ_+ and the antisymmetric excited state Ψ_- for a particle in a double-well potential [Fic07].

Usually the zero-energy point is chosen between the two levels and thus the eigenvalues of Ψ_+ and Ψ_- take on the values of $-E/2$ and $+E/2$ respectively. As a consequence, the Hamiltonian of the two-level system can now be defined in the basis of its eigenstates (Ψ_+, Ψ_-) as

$$H_0' = \frac{1}{2} \begin{pmatrix} E & 0 \\ 0 & -E \end{pmatrix}. \tag{2.11}$$

As is shown in [Esq98], the Hamiltonian in the basis of the isolated wells can also be transformed into the eigenstate basis of the two-level system via diagonalisation by a rotation matrix.

The Hamilton operator H_0' in (2.11) can alternatively be expressed as $H_0' = \frac{E}{2}\sigma_z$ with Pauli matrix $\sigma_z = \begin{pmatrix} 1 & 0 \\ 0 & -1 \end{pmatrix}$ and is equivalent to the operator of a magnetic dipole with spin $1/2$ in a static magnetic field. This analogy is very interesting because it shows, as is brilliantly explained in [Fey57], that any two-level system can be described by the same formalism.

A useful quantity of a two-level system is its occupation difference which can be derived in the framework of statistical physics. By setting the energy of the ground state to zero and thus the energy of the excited state to E, the partition function of a single two-level system is given by

$$Z = \sum_{i=0}^{n} e^{-E_i/k_B T} = 1 + e^{-E/k_B T}. \tag{2.12}$$

The occupation probability of any given energy level is defined as

$$P(E_i) = \frac{1}{Z}\exp(-E_i/k_B T) \tag{2.13}$$

and hence the occupation difference $\Delta P = P(0) - P(E)$ equals to

$$\Delta P = \frac{1}{Z}\left(1 - \mathrm{e}^{-E/k_\mathrm{B}T}\right) = \frac{1 - \mathrm{e}^{-E/k_\mathrm{B}T}}{1 + \mathrm{e}^{-E/k_\mathrm{B}T}} = \frac{\mathrm{e}^{E/k_\mathrm{B}T} - 1}{\mathrm{e}^{E/k_\mathrm{B}T} + 1} = \tanh\left(\frac{E}{2k_\mathrm{B}T}\right). \tag{2.14}$$

The occupation difference depends thus on the energy splitting E and the temperature T. Similarly, for N independent, non-interacting two-level systems in thermal equilibrium, the difference in occupation is given as

$$\frac{\Delta N}{N} = \tanh\left(\frac{E}{2k_\mathrm{B}T}\right). \tag{2.15}$$

2.2.2 Distribution function of the tunnelling parameters

In amorphous solids, due to the disorder of the structure, the double-well potential of the tunnelling systems can exist in a variety of shapes. This is taken into consideration in the standard tunnelling model by implying that the parameters Δ, V, d and m are broadly distributed. Additionally, the model also assumes that the asymmetry energy Δ and the tunnelling parameter λ are independent of each other and equally distributed. Their distribution function is given by

$$P(\lambda, \Delta)\,\mathrm{d}\lambda\,\mathrm{d}\Delta = \overline{P}\,\mathrm{d}\lambda\,\mathrm{d}\Delta \tag{2.16}$$

where $\overline{P}$ is a material specific constant. Since tunnelling systems with a well-defined energy splitting E are excited during the high-frequency measurements presented in the framework of this report, it is advantageous to express the distribution function in terms of E and the tunnel splitting Δ_0. This is done via a Jacobian transformation while making use of $\Delta_0 = \hbar\Omega\,\mathrm{e}^{-\lambda}$ and $E = \sqrt{\Delta^2 + \Delta_0^2}$

$$P(E, \Delta_0)\,\mathrm{d}\Delta_0\,\mathrm{d}E = P(\Delta, \lambda)\left|\frac{\partial\lambda}{\partial\Delta_0}\right|\left|\frac{\partial\Delta}{\partial E}\right|\mathrm{d}\Delta_0\,\mathrm{d}E$$

$$= \overline{P}\,\frac{E}{\Delta_0\sqrt{E^2 - \Delta_0^2}}\,\mathrm{d}\Delta_0\,\mathrm{d}E. \tag{2.17}$$

Alternatively, the distribution function can also be expressed in terms of E and Δ

$$P(E, \Delta)\,\mathrm{d}\Delta\,\mathrm{d}E = \overline{P}\,\frac{E^2}{E^2 - \Delta^2}\,\mathrm{d}\Delta\,\mathrm{d}E. \tag{2.18}$$

By analysing the distribution function of the tunnel splitting and the asymmetry energy, it is possible to discern which tunnelling systems are most likely to be present in an amorphous structure. Since only tunnelling systems with a certain constant energy splitting E are excited, the most information is gained by looking at the probability distributions $P(\Delta_0/E, E = \mathrm{const.})$ and $P(\Delta/E, E = \mathrm{const.})$ plotted against Δ/E as represented in Figure 2.7.
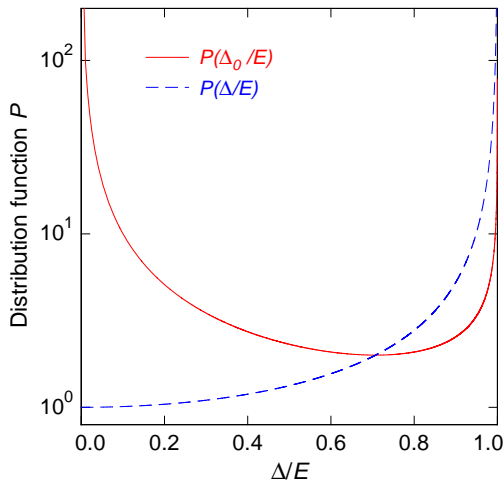
Figure 2.7: Distribution function of the tunnel splitting Δ_0 (straight line) and asymmetry energy Δ (dashed line) for a constant energy splitting E as predicted by the standard tunnelling model [Fic13]. Quantities that depend on Δ_0/E can be respresented with $\frac{\Delta_0}{E} = \sqrt{1 - \left(\frac{\Delta}{E}\right)^2}$ according to equation (2.7).

The totally symmetric tunnelling systems ($\Delta/E \rightarrow 0$) are located to the left while the totally antisymmetric ones ($\Delta/E \rightarrow 1$) can be found to the right in the graph. The distribution $P(\Delta_0/E)$ shows a divergence for symmetric as well as antisymmetric tunnelling systems. This means that the probability of a tunnelling process is high for symmetric as well as antisymmetric tunnelling systems but only if the amount of the latter is sufficiently high. Physical quantities that depend on Δ_0/E like the Rabi frequency (see section 2.3.2) as well as the resonant interaction between tunnelling systems and phonons (see section 2.4) are hence defined by tunnelling systems in the limits of small and large asymmetry energies Δ.

The probability distribution $P(\Delta/E)$ also diverges for antisymmetric tunnelling systems but converges to 1 for $\Delta/E \rightarrow 0$. Physical processes that depend on Δ/E, like the spectral diffusion (see section 2.4), are thus defined mainly by very antisymmetric tunnelling systems.

At first glance the constant probability distribution of the standard tunnelling model (2.16) seems like a crude approximation. The derivation of the specific heat, however, confirms its validity. The density of states is calculated by integrating (2.17) over Δ_0

$$D(E) = \int\limits_{\Delta_{0,\mathrm{min}}}^{E} P(E, \Delta_0) \, \mathrm{d}\Delta_0 = \overline{P} \ln\left(\frac{2E}{\Delta_{0,\mathrm{min}}}\right) \tag{2.19}$$

where a minimal $\Delta_{0,\mathrm{min}}$ is introduced to avoid a non-integrable divergence as well as to account for the possibility that there might be a maximal potential barrier height. From the density of states, the specific heat can be determined to vary linearly with temperature [Ens05]. By looking at the specific heat of amorphous silica in Figure 2.1 however, the temperature dependence is not exactly linear. As is explained in [Zim81], the real temperature dependence of the specific heat is better described by $C \propto T^{1+\alpha}$ with $\alpha \ll 1$ and is due to the distribution of the thermal relaxation times in tunnelling systems

as well as finite measurement times.

2.2.3 Interaction between tunnelling systems and alternating electric fields

In thermal equilibrium, the tunnelling systems can be described by their unperturbed Hamiltonian H_0 (2.9). An applied alternating electric field $\boldsymbol{F} = \boldsymbol{F_0}\cos(\omega_{\mathrm{EF}}t)$ can couple to the dipole moments $\boldsymbol{p}$ of the tunnelling systems and cause a variation of their asymmetry energy and tunnel splitting. The electric field can thus be seen as a pertubation and, if sufficiently small, have its effects described by first-order perturbation theory. It is assumed that a weak field does not alter the potential barrier V nor the distance d which is why the variation of the tunnel splitting $\delta\Delta_0$ is negligable compared to the variation of the asymmetry energy $\delta\Delta$ [Phi81]. The resulting perturbation Hamiltonian is given by

$$H_{\mathrm{S}} = \frac{1}{2}\begin{pmatrix} \delta\Delta & -\delta\Delta_0 \\ -\delta\Delta_0 & -\delta\Delta \end{pmatrix} \approx \frac{1}{2}\begin{pmatrix} \delta\Delta & 0 \\ 0 & -\delta\Delta \end{pmatrix}. \tag{2.20}$$

The variation of the asymmetry energy $\delta\Delta$ equates to the variation of the potential energy due to the interaction between dipole moment $\boldsymbol{p}$ and alternating electric field $\boldsymbol{F}$

$$H_{\mathrm{S}} = \frac{1}{2}\begin{pmatrix} \delta\boldsymbol{p}\cdot\boldsymbol{F} & 0 \\ 0 & -\delta\boldsymbol{p}\cdot\boldsymbol{F} \end{pmatrix}. \tag{2.21}$$

Transforming the perturbation Hamiltonian into the basis of the eigenstates of the tunnelling systems (Ψ_+, Ψ_-) yields

$$H_{\mathrm{S}}' = \frac{1}{2E}\begin{pmatrix} \Delta & \Delta_0 \\ \Delta_0 & -\Delta \end{pmatrix}\delta\boldsymbol{p}\cdot\boldsymbol{F}. \tag{2.22}$$

The diagonal elements describe the change in the energy splitting caused by the external field while the off-diagonal elements give rise to transitions between the two energy levels. Finally the total Hamiltonian reads

$$H' = H_0' + H_{\mathrm{S}}' = \frac{1}{2}\begin{pmatrix} E & 0 \\ 0 & -E \end{pmatrix} + \underbrace{\frac{1}{2E}\begin{pmatrix} \Delta & \Delta_0 \\ \Delta_0 & -\Delta \end{pmatrix}\delta\boldsymbol{p}}_{\boldsymbol{P}'}\cdot\boldsymbol{F_0}\cos(\omega_{\mathrm{EF}}t) \tag{2.23}$$

where $\boldsymbol{P}'$ is the polarisation operator.

2.2.4 Shortcomings of the standard tunnelling model

Due to being able to describe the temperature dependence of the specific heat and other acoustic and dieletric properties reasonably well [Phi81], the standard tunnelling model has established itself as the basic theoretical framework for the interpretation of experimental studies on glasses at low temperatures.

Unfortunately, the model also presents some deficiencies, one of which is shown in Figure 2.8 where the relative change of the capacitance of a capacitor filled with the glass BK7 is plotted against temperature. The measured quantity $\Delta C/C$ is proportional to the relative change of the real part of the dielectric function $\delta\epsilon/\epsilon$ for which the standard tunnelling model predicts a -2:1 slope ratio in logarithmic representation. The experiment, however, reveals a slope ratio much closer to -1:1 [Ens90] [Woh01]. The same phenomenon has also been observed in measurements of the relative change of the sound velocity in vitreous silica [Cla00]. The reason for this discrepancy has not yet been understood but might have its origin in the interaction between tunnelling systems which is not taken into account in the standard tunnelling model. This interaction, encompassed in the model of spectral diffusion (see section 2.4), is necessary to explain certain phenomena such as the decay of polarisation echoes.
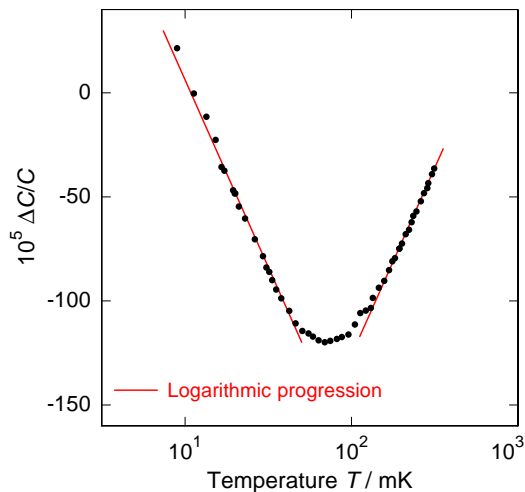
Figure 2.8: Relative change of the capacitance of the glass BK7 at a frequency of $1\,\mathrm{kHz}$ and a field strength of $75\,\mathrm{V/m}$ as a function of temperature [Woh01].
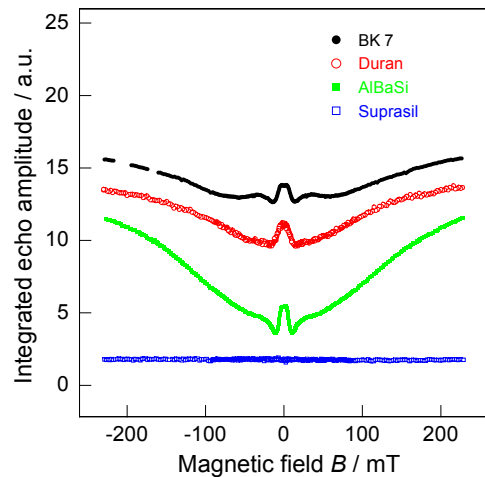
Figure 2.9: Magnetic field dependence of the amplitude of spontaneous polarisation echoes in the BK7, BaO-Al$_2$O$_3$-SiO$_2$ (AlBaSi), Duran and Suprasil I glasses [Lud03].

Another flaw of the standard tunnelling model is that it fails to predict the magnetic field dependence of certain quantities [Str98] [Lud02] [Lud03]. As an example, Figure 2.9 shows the echo amplitude of two-pulse polarisation echoes measured under the influence of a magnetic field in the range from -200 mT to 200 mT for four different glasses [Lud03]. Even though these glasses are non-magnetic, three of them show a pronounced magnetic field dependence while only Suprasil I, i.e. vitreous silica containing $1200\,\mathrm{ppm}\,\mathrm{OH}^-$, seems to be independent of the magnetic field. This phenomenon can be explained by the nuclear quadrupole effect which states that tunnelling particles with electric and magnetic nuclear moments can interact with the local electric field gradient leading to a quadrupole splitting of their energy levels [Wue02]. Magnetic fields can cause an additional Zeeman splitting

of these levels giving rise to interference effects which then in turn cause the magnetic field dependence of the echo amplitude. This explanation is supported by the fact that Suprasil I does not carry any nuclear quadrupole moments while the other three glasses do. The nuclear quadrupole effect is treated separately in section 2.5.
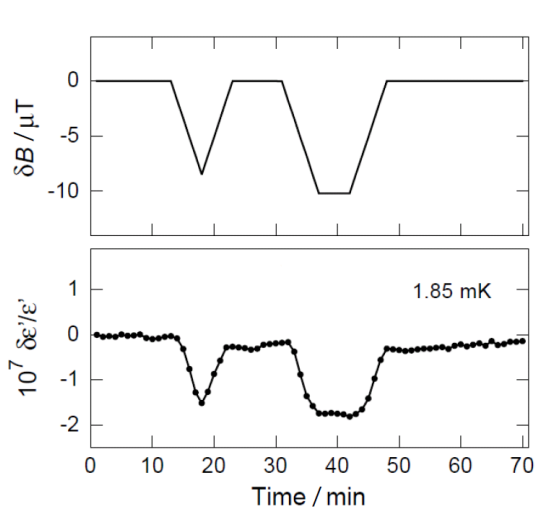
Figure 2.10: Magnetic field dependence of the dielectric constant in the BaO-Al$_2$O$_3$-SiO$_2$ glass [Str98]. The top part of the figure shows the time variation of the applied field while the bottom part shows the response of the dielectric constant to the field at 1.85 mK.
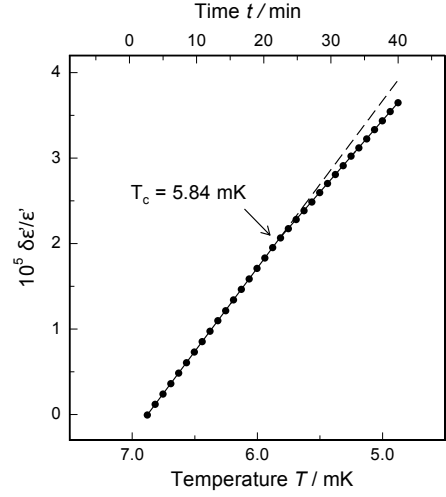
Figure 2.11: Relative change of the dielectric permittivity of BaO-Al$_2$O$_3$-SiO$_2$ plotted against temperature and time. The dashed line represents the extrapolation of the data from higher temperatures [Str98].

In addition to polarisation echoes, a magnetic field dependence of the dielectric constant of the BaO-Al$_2$O$_3$-SiO$_2$ glass has also been observed. In fact, it has been shown that magnetic fields up to 20 T at temperatures down to 16 mK have no perceptible effect on the dielectric constant of the BaO-Al$_2$O$_3$-SiO$_2$ glass. Measurements of Strehlow et al. however prove that, below a temperature of approximately 5 mK and for very small magnetic field strengths, the dielectric constant exhibits a magnetic field dependence [Str98]. In this context, Figure 2.10 shows the relative change of the dielectric constant in the presence of a varying magnetic field plotted as a function of time at 1.85 mK. The dielectric constant clearly follows the variation of the magnetic field. Similar effects have been observed for the same type of measurement at different temperatures up to 5.07 mK.

In a further experiment, the dielectric constant was measured while the BaO-Al$_2$O$_3$-SiO$_2$ glass was cooled down from 6.88 mK to 4.88 mK at a constant rate of 62.6 μK/min. The result can be seen in Figure 2.11. The relative change of the dielectric function shows a sudden change of its slope at $T_c = 5.84$ mK indicating a possible phase transition. It is assumed that this continuous phase transition leads, from the previously uncorrelated and

incoherent tunnelling motion of the individual interacting tunnelling systems at higher temperatures, to a coherent and collective tunnelling motion with minimal interaction energy below T_c. The same type of measurement has been reproduced in other multicomponent glasses resulting in similar findings [Str98].

To sum up, it is fair to say that the standard tunnelling model is able to describe the macroscopic behaviour of amorphous solids reasonably well. However, its biggest shortcoming is that it fails to deliver a microscopic picture of the tunnelling systems. Recently, first time detailed conclusions about the microscopic nature of the tunnelling systems in amorphous glycerol could be drawn through polarisation echo experiments [Bar13].
Thus, two-pulse polarisation echoes, an appriopriate measurement method to study the interaction between tunnelling systems, can be used in an attempt to answer some of the questions concerning the microscopic nature of the tunnelling systems.

2.3   Polarisation echoes

2.3.1   Phenomenological description

At very low temperatures where the thermal energy of the tunnelling systems is smaller than the energy splitting of the two lowest energy states, the tunnelling systems can effectively be described as two-level systems. By resonantly exciting the two-level systems via short pulses of microwave radiation, it is possible to induce transitions from the ground state into a mixing state of the two energy levels which ultimately results in a macroscopic polarisation. This phenomenon is based on the coherent behaviour of the tunnelling systems and is only guaranteed at sufficiently low temperatures where relaxation processes, destroying the phase coherence of the tunnelling sytems, are only taking place slowly.

During the measurement, the tunnelling systems are excited by a sequence of very short high-frequency electric pulses. If the energy splitting $E = \hbar\omega_{\mathrm{TS}}$ is approximately equal to the energy of the alternating electric field $\hbar\omega_{\mathrm{EF}}$, there is resonant interaction between tunnelling systems and electric field. Depending on which properties of the material are being investigated, a specific sequence with a certain amount of pulses of different durations can be used. The two-pulse sequence, used in the framework of this thesis and shown in the top part of Figure 2.12, investigates the T_2 relaxation mechanism of tunnelling systems (see section 2.4). The pulses, indicated by the grey rectangles, as well as the answer of the system i.e. the polarisation, portrayed as red area, are represented as a function of time. The pulses are assumed to be much shorter than the pulse separation time τ_{12}. In the bottom part of Figure 2.12, the corresponding temporal evolution of the system is visually represented in a so-called path diagram.
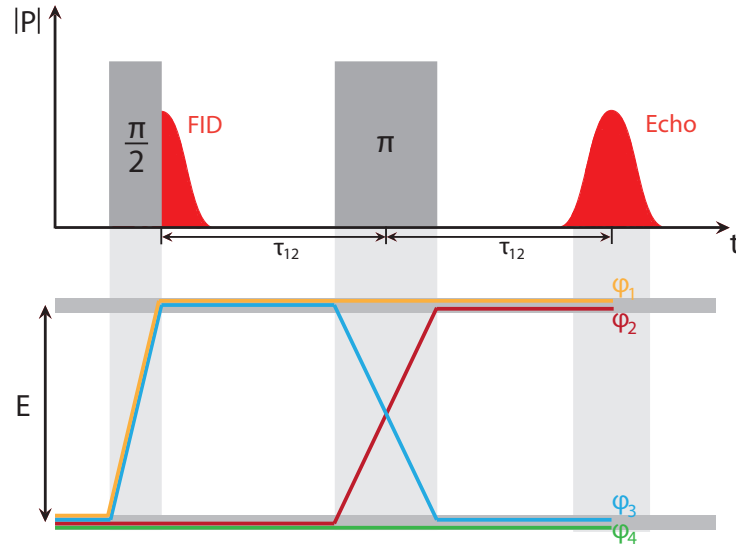
Figure 2.12: Top: Schematic representation of the pulse sequence of a two-pulse polarisation echo measurement showing the polarisation amplitude (red) and the pulses (grey) as a function of time. **Bottom:** Path diagram showing the temporal evolution of the states of a single two-level system with energy splitting E. The different possible evolutions are represented in different colors. The quantum mechanical phase gathered by the different paths equates to the area enclosed by the corresponding path.

Prior to the application of the first pulse the sample is in thermal equilibrium. Since the thermal energy is much lower than the energy splitting, most tunnelling systems are in the ground state Ψ_+. With the wavefunction of the ground state being symmetric, the tunnelling particles are delocalised and the average dipole moment of each tunnelling system is zero. The first high-frequency pulse, of duration t_1 and labelled as $\frac{\pi}{2}$-pulse, mixes the states of the tunnelling systems and puts them into a superposition state of the ground state Ψ_+ and the excited state Ψ_-. As can be deduced from Figure 2.6, this mixing leads to the localisation of the tunnelling particles in either the left ($\Psi_+ + \Psi_-$) or the right (Ψ_+ - Ψ_-) well which in turn results in the formation of an average dipole moment. In the bottom part of Figure 2.12, the mixing of the states is illustrated by the transition of the orange and blue lines to the upper level. In a microscopic picture, the pulse initiates a coherent back-and-forth tunnelling motion of the particles between the two wells.

Since in a glass a large amount of tunnelling systems are excited by the alternating electric field, the resulting aligned dipole moments form an oscillating macroscopic polarisation. After switching off the electric field, every tunnelling system evolves freely in time by continuing to oscillate with its eigenfrequency $\omega_{\text{TS}} = E/\hbar$. A large amount of tunnelling systems with different energy splittings are excited because of the short duration of the pulse (several hundred nanoseconds) which, according to the uncertainty principle $\Delta E \Delta t \geq \hbar/2$, leads to a high energy blurring (portrayed by the shading of the energy levels in the path diagram in Figure 2.12). As a consequence, not all tunnelling systems

share the same energy splitting and thus eigenfrequency, and are quickly beginning to oscillate out of phase which leads to a decay of the macroscopic polarisation. This effect is known as 'Free Induction Decay (FID)'.

After the pulse separation time τ_{12} of free evolution, a second pulse of double duration t_2 and thus labelled as π-pulse is sent in, leading to a new mixing of the states. Afterwards, the system is again evolving freely in time. For a two-level system exactly four different evolutions to ultimate states are possible. Since tunnelling systems are of quantum mechanical nature, the total state is a superposition of these four states with each having a different probability. At a time $t = 2\tau_{12}$, the states represented by the red and blue line share the same phase as was the case immediately after the first pulse. The result is once again a macroscopic polarisation and is called 'spontaneous echo' or 'two-pulse echo'. The remaining two states (orange and green lines) possess a different phase and thus don't contribute to the echo. In order to get an optimal echo signal, it is necessary to suppress these non-contributing states. As will be shown during the quantum mechanical description of the polarisation echoes further below, this is done by choosing an appropriate pulse form.

Alternatively, the temporal evolution of the system can be visualised with the help of the Bloch sphere, a well-known geometrical representation of two-level quantum mechanical systems and used for the description of nuclear magnetic resonance (NMR). As already mentioned in section 2.2.1, tunnelling systems as well as spin-1/2 particles in a constant magnetic field can be described by the same formalism. Applying an alternating electric field to tunnelling systems equates to applying a weak alternating magnetic field to spin-1/2 particles which is exactly what is done in nuclear magnetic resonance experiments. Thus, in analogy to the formation of Hahn echoes in NMR, the formation of polarisation echoes can also be explained by making use of so-called 'pseudospin vectors' describing the states inside the Bloch sphere in 'pseudospin space'.

In this context Figure 2.13 shows the temporal evolution of the system in a series of Bloch spheres. The z-component corresponds to the occupation difference of the tunnelling systems. If the net pseudospin vector $\boldsymbol{S}$ points downwards along the z-axis, the tunnelling systems are in their ground state Ψ_+, while pointing upwards along the axis indicates the occupation of the excited state Ψ_-. Any other state denotes a mixed state of both energy levels. The y-component corresponds to the polarisation. The larger the magnitude of $\boldsymbol{S}$ in the y-direction, the more the tunnelling systems contribute to the macroscopic polarisation. The x-axis is related to the quantum mechanical phase of the system. At the beginning, the tunnelling systems are in their ground state and the pseudospin vector $\boldsymbol{S}$ points downwards along the z-axis (Figure 2.13a). Applying an alternating electric field leads to a precession of $\boldsymbol{S}$ around the z-axis with frequency ω_{EF}. In order to get rid of this precession, the coordinate system is put into an alternative frame of reference rotating around the z-axis with angular velocity ω_{EF}. The first pulse of duration t_1 leads to a macroscopic polarisation by rotating the pseudospin vector around the x-axis by 90° and
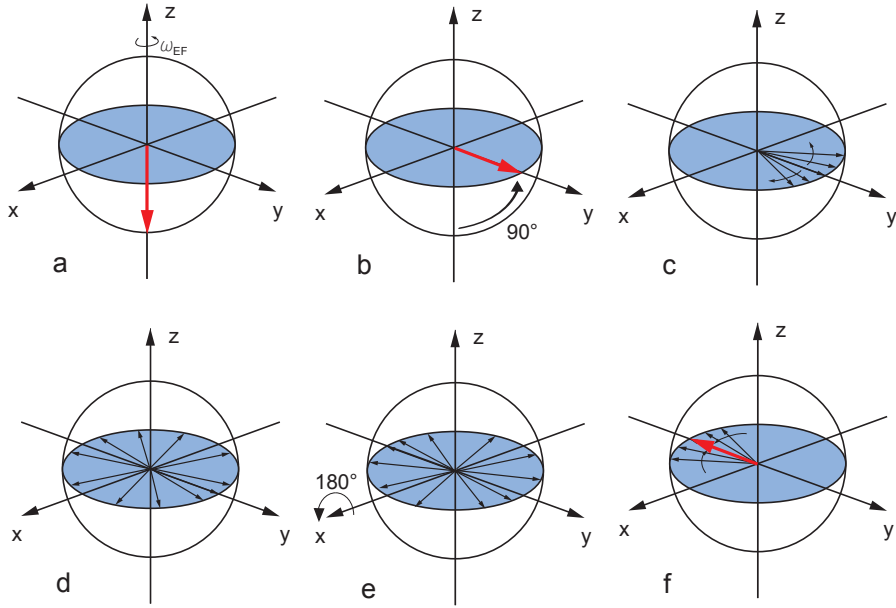
Figure 2.13: Schematic representation of the temporal evolution of an ensemble of tunnelling systems driven by a pulse sequence and represented in a series of Block spheres. **a**: $t = 0$, system in the ground state. **b**: $t = t_1$, end of the first pulse. **c**: $t \geq t_1$, free induction decay. **d**: $t_1 < t < \tau_{12}$, statistical distribution of the individual pseudospins in the $x - y$ plane. **e**: $t = \tau_{12}$, application of the second pulse. **f**: $t = 2\tau_{12}$, spontaneous echo. The figure is provided through the courtesy of Christian Schötz.

thus aligning it along the y-axis (Figure 2.13**b**). After switching off the electric field, the individual tunnelling systems are dephasing according to their eigenfrequency ω_{TS} leading to the free induction decay. In the rotating frame of reference, the pseudospins rotate with different speeds both clockwise and anticlockwise around the z-axis (Figure 2.13**c** to Figure 2.13**d**). After the time τ_{12}, the application of the second pulse of duration t_2 rotates the pseudospin vectors around the x-axis by 180° leading to an inversion of the rotation of the individual pseudospins (Figure 2.13**e**) and thus to a time inversion of their phase evolution. After a time $2\tau_{12}$, the individual pseudospins have all lined up with each other again in the opposite direction on the y-axis resulting in the spontaneous echo.

2.3.2 Quantum mechanical description

After the phenomenological description of the two-pulse polarisation echoes, their quantitative behaviour is now explicitly calculated. The derivation follows the thought process laid out in [Klo08] and [Rue08].

In the following it is assumed that the tunnelling systems are in the ground state prior to the application of the pulse sequence. Additionally the tunnelling systems can be seen as quasi-isolated which means that every tunnelling system contributes separately to the

echo. The total polarisation can then be obtained by summing over all tunnelling systems. The total wavefunction of a single tunnelling system is defined by the superposition of the symmetric and antisymmetric wavefunctions

$$\Psi = c_1(t)\Psi_+ + c_2(t)\Psi_- \tag{2.24}$$

with time-dependent coefficients $c_1(t)$ and $c_2(t)$ of the ground state and excited state respectively. The temporal evolution of the system can be studied by applying the total Hamiltonian (2.23) to the total wavefunction. However, in a first step, as already mentioned during the phenomenological description of the polarisation echoes, it is useful to transform the coordinate system into a rotating frame of reference with frequency ω_{EF}. The total Hamiltonian is then modified according to

$$H'' = \mathrm{e}^{\mathrm{i}\omega_{\mathrm{EF}}t\sigma_z}\, H'\, \mathrm{e}^{-\mathrm{i}\omega_{\mathrm{EF}}t\sigma_z} - \hbar\omega_{\mathrm{EF}}\sigma_z \tag{2.25}$$

where the second term represents a correction term nullifying the acceleration caused by the rotation. The modified polarisation operator remains largely unaffected and still shows the following proportionality

$$\boldsymbol{P}'' \propto \frac{1}{E}\begin{pmatrix} \Delta & \Delta_0 \\ \Delta_0 & -\Delta \end{pmatrix}. \tag{2.26}$$

The echo amplitude equates to the expectation value of the polarisation operator

$$\langle \boldsymbol{P}'' \rangle = \langle \Psi | \, \boldsymbol{P}'' \, | \Psi \rangle. \tag{2.27}$$

Hence it necessary to determine the coefficients $c_1(t)$ and $c_2(t)$ at a time $t > \tau_{12}$. Prior to the application of the first pulse, the tunnelling system is in its ground state

$$\begin{aligned} c_1(0) &= 1 \\ c_2(0) &= 0. \end{aligned} \tag{2.28}$$

The first pulse leads to the mixing of the energy states which is described by the off-diagonal elements of H''. However in the rotating frame of reference, H'' does not show an explicit time dependence which is why the temporal evolution of the tunnelling system can be described by time propagators $\mathrm{e}^{-\mathrm{i}H''t/\hbar}$. During the duration t_1 of the first pulse, the system is governed by the propagator

$$\mathrm{e}^{-\mathrm{i}\frac{\Omega_{\mathrm{R}}t}{2}\sigma_x} = \mathbb{1}\cos\frac{\Omega_{\mathrm{R}}t}{2} - \mathrm{i}\,\sigma_x\sin\frac{\Omega_{\mathrm{R}}t}{2} \tag{2.29}$$

with unity matrix $\mathbb{1}$, Pauli matrix $\sigma_{\mathrm{x}} = \begin{pmatrix} 0 & 1 \\ 1 & 0 \end{pmatrix}$ and Rabi frequency

$$\Omega_{\mathrm{R}} = \frac{\delta\boldsymbol{p}\,\mathbf{F_0}}{\hbar}\left(\frac{\Delta_0}{E}\right). \tag{2.30}$$

The Rabi frequency describes the rate at which the population between the two levels varies. Right after the first pulse the coefficients yield

$$
\begin{aligned}
c_1(t_1) &= \cos\frac{\Omega_R t_1}{2} \\
c_2(t_1) &= -i\sin\frac{\Omega_R t_1}{2}
\end{aligned}
\tag{2.31}
$$

where the pulse duration t_1 is chosen to be much shorter than the pulse separation $t_1 \ll \tau_{12}$. After switching off the electric field, the tunnelling system evolves freely in time. The coefficients are then governed by the propagator

$$
e^{-i\frac{\omega_d t}{2}\sigma_z} = \mathbb{1}\cos\frac{\omega_d t}{2} - i\sigma_z\sin\frac{\omega_d t}{2}
\tag{2.32}
$$

stemming from the diagonal elements of the rotating unperturbed Hamiltonian H_0''. To account for the rotation which is now relevant since the electric field has been switched off, the frequency difference $\omega_d = \omega_{TS} - \omega_{EF}$ has been introduced. Before the application of the second pulse i.e. at a time $t_1 < t < \tau_{12}$ the coefficients have the form

$$
\begin{aligned}
c_1(t) &= \cos\frac{\Omega_R t_1}{2}\, e^{-i\frac{\omega_d}{2}t} \\
c_2(t) &= -i\sin\frac{\Omega_R t_1}{2}\, e^{i\frac{\omega_d}{2}t} \; .
\end{aligned}
\tag{2.33}
$$

Afterwards, the second pulse of duration t_2 is applied and the evolution of the system can again be described by the propagator (2.29). Immediately after the second pulse $t = t_1 + \tau_{12} + t_2$, the coefficients are

$$
\begin{aligned}
c_1(t_1+\tau_{12}+t_2) &= \cos\frac{\Omega_R t_2}{2}\cos\frac{\Omega_R t_1}{2}\, e^{-i\frac{\omega_d}{2}\tau_{12}} - \sin\frac{\Omega_R t_2}{2}\sin\frac{\Omega_R t_1}{2}\, e^{i\frac{\omega_d}{2}\tau_{12}} \\
c_2(t_1+\tau_{12}+t_2) &= -i\sin\frac{\Omega_R t_2}{2}\cos\frac{\Omega_R t_1}{2}\, e^{-i\frac{\omega_d}{2}\tau_{12}} - i\cos\frac{\Omega_R t_2}{2}\sin\frac{\Omega_R t_1}{2}\, e^{i\frac{\omega_d}{2}\tau_{12}} \; .
\end{aligned}
\tag{2.34}
$$

Afterwards, the system is once again evolving freely in time. Since a macroscopic polarisation occurs immediately after the first pulse t_1 and at $t = 2\tau_{12}$, the phase of the system has to be identical at these two points in time. This is ensured by applying the propagator

$$
e^{-i\frac{\omega_d}{2}(t-\tau_{12})\sigma_z}
\tag{2.35}
$$

to the coefficients. Finally, at a time $t > \tau_{12}$ the coefficients have the form

$$
\begin{aligned}
c_1(t>t_{12}) &= {} = \cos\frac{\Omega_R t_1}{2}\cos\frac{\Omega_R t_2}{2}\, e^{-i\frac{\omega_d}{2}t} - \sin\frac{\Omega_R t_1}{2}\sin\frac{\Omega_R t_2}{2}\, e^{-i\frac{\omega_d}{2}(t-2\tau_{12})} \\
c_2(t>t_{12}) &= {} = -i\sin\frac{\Omega_R t_2}{2}\cos\frac{\Omega_R t_1}{2}\, e^{i\frac{\omega_d}{2}(t-2\tau_{12})} - i\sin\frac{\Omega_R t_1}{2}\cos\frac{\Omega_R t_2}{2}\, e^{i\frac{\omega_d}{2}t} \; .
\end{aligned}
\tag{2.36}
$$

The two coefficients possess four different terms which correspond to the four different states in Figure 2.12. The first term of $c_1(t)$ corresponds to the green line with no mixing of the energy levels while the second term corresponds to the blue line with mixing up to the upper level due to the first pulse and subsequent mixing down to the lower level due to the second pulse. The first term of $c_2(t)$ corresponds to the orange line with mixing up due to the first pulse whereas the second term corresponds to the red line with mixing up due to the second pulse only.

With the above result and by considering (2.26), it is now possible to calculate the expectation value of the polarisation operator

$$\langle \boldsymbol{P}'' \rangle = \frac{1}{E} \left(c_1^* c_1 \Delta + c_1^* c_2 \Delta_0 + c_2^* c_1 \Delta_0 - c_2^* c_2 \Delta \right). \tag{2.37}$$

The diagonal elements, i.e. the first and fourth summand, yield a time-independent contribution that is averaged out due to the broad distribution of Δ and Δ_0. The remaining off-diagonal elements yield the time-dependent phase factors $e^{\pm i \omega_d t}$, $e^{\pm i \omega_d (t - \tau_{12})}$ and $e^{\pm i \omega_d (t - 2\tau_{12})}$. Since the eigenfrequency ω_{TS} of the tunnelling systems is broadly distributed, the same holds true for ω_d. Thus, for $t > \tau_{12}$, the terms with phase factors $e^{\pm i \omega_d t}$ and $e^{\pm i \omega_d (t - \tau_{12})}$ are negligible. Finally the expectation value of the polarisation has the form

$$\langle \boldsymbol{P}''(t > \tau_{12}) \rangle \propto \frac{\Delta_0}{E} \sin \frac{\Omega_R t_1}{2} \sin^2 \frac{\Omega_R t_2}{2} \cos \frac{\Omega_R t_1}{2} \left[e^{i \omega_d (t - 2\tau_{12})} + e^{-i \omega_d (t - 2\tau_{12})} \right] \tag{2.38}$$

and effectively consists solely of the states portrayed by the red and blue line in Figure 2.12. It is evident that for $t = 2\tau_{12}$ the phase factor vanishes independently of ω_d. This means that every resonant tunnelling system, no matter the eigenfrequency ω_{TS}, contributes to the echo. The phase-independent echo amplitude can further be maximised if the pulses fulfill the conditions $\Omega_R t_1 = \frac{\pi}{2}$ and $\Omega_R t_2 = \pi$, which is why the pulse sequence is called $\frac{\pi}{2}$-π sequence. By looking at (2.36), it is clear that the $\frac{\pi}{2}$-π pulse sequence leads to the first term of c_1 and the second term of c_2 being zero and thus effectively suppresses the contribution of the phase-dependent states, portrayed by the orange and green line in Figure 2.12, to the echo. The $\frac{\pi}{2}$-π condition can be fulfilled by choosing both an appriopriate pulse length and pulse height i.e. field strength.
Additionally, by assuming very short pulse lengths such that $t_1 \approx t_2 \approx t_p$, the echo amplitude is given by

$$\langle \boldsymbol{P}''(t > t_{12}) \rangle = A_{echo} \propto \frac{\Delta_0}{E} \left(\frac{\Omega_R t_p}{2} \right)^3 \propto \left(\frac{\Delta_0}{E} \right)^4. \tag{2.39}$$

From this result it is evident that symmetric tunnelling systems, i.e. those with large Δ_0 and small Δ, contribute more to the echo amplitude than antisymmmetric ones. However, equation (2.39) only shows the echo ampltiude of a single tunnelling system with a specific tunnel splitting Δ_0. In order to determine the echo amplitude of the whole ensemble of tunnelling systems, (2.39) has to be integrated over all values of Δ_0 whilst using the distribution function proposed by the standard tunnelling model.

The phenomenological description as well as the quantum mechanical calculation suggest that the initial polarisation right after the first pulse is identical to the final echo since the resonant tunnelling systems are again aligned in phase at $t = 2\tau_{12}$. Experiments, however, have shown that this is not the case. In fact, the larger the pulse separation τ_{12}, the smaller the final echo amplitude. This reduction or decay can be attributed to relaxation mechanisms which destroy the phase coherence of the tunnelling systems. The

larger τ_{12}, the higher the probability a tunnelling system loses its phase coherence and thus fails to contribute to the echo. These relaxation mechanisms are covered in the following section.

2.4 Relaxation and spectral diffusion

In total one distinguishes between two different relaxation processes. The longitudinal relaxation process describes the time an ensemble of tunnelling systems requires to reach thermal equilibrium after an external perturbation. This relaxation consists of transitions from the upper into the lower energy state resulting in the emission of thermal phonons. This means that resonantly-excited tunnelling systems will decay back into the ground state and are thus unable to contribute to the echo.

At very low temperatures, i.e. below $1\,\mathrm{K}$, the interaction between tunnelling systems and the phonon bath is described by single-phonon processes [Jae72]. The corresponding relaxation rate T_1^{-1} can be obtained via Fermi's golden rule

$$T_1^{-1} = \left(\frac{\gamma_\ell^2}{v_\ell^5} + \frac{2\gamma_{\mathrm{t}}^2}{v_{\mathrm{t}}^5} \right) \left(\frac{\Delta_0}{E} \right)^2 \frac{E^3}{2\pi\rho\hbar^4} \coth\left(\frac{E}{2k_{\mathrm{B}}T} \right) \tag{2.40}$$

where ρ denotes the density, γ is the elastic deformation potential and v is the speed of sound. The indices ℓ and t denote the longitudinal and the transversal phonon branch respectively. With $T_1^{-1} \propto \Delta_0^2$, the relaxation rate is broadly distributed and high for symmetric tunnelling systems. Additionally, the relaxation rate depends on the temperature through the population factor $\coth\left(\frac{E}{2k_{\mathrm{B}}T} \right)$ and increases for increasing temperatures. At sufficiently high temperatures such that $E \leq k_{\mathrm{B}}T$ the population factor varies linearly with temperature. As a result the relaxation time is inversely proportional to the temperature

$$T_1 \propto T^{-1} \tag{2.41}$$

The minimal longitudinal relaxation time $T_{1,\mathrm{min}}$ typically lies in the range of several 100 microseconds at $T \approx 10\,\mathrm{mK}$ [Fic13].

The longitudinal relaxation mechanism leads to an exponential decay of the echo amplitude which can be described by the factor $\exp(-t/T_1)$. Writing the relaxation rate (2.40) as $T_1^{-1} = T_{1,\mathrm{min}}^{-1}[1 - (\frac{\Delta}{E})^2]$, the contribution of the longitudinal relaxation to the echo amplitude at the time $t = 2\tau_{12}$ is given by

$$W_{\mathrm{R}}(2\tau_{12}) = \exp\left[-2\tau_{12}\, T_{1,\mathrm{min}}^{-1} \left(1 - \left(\frac{\Delta}{E} \right)^2 \right) \right]. \tag{2.42}$$

The transversal relaxation mechanism describes the interaction between resonant tunnelling systems and their surrounding environments. Variations in the elastic field lead to a shift in the energy splitting of the resonant tunnelling systems. As a result they lose

their phase coherence and are unable to contribute towards the echo. These processes
are characterised by the transversal relaxation time T_2 and are described in the model of
spectral diffusion in [KA62] and [BH77].

At temperatures below $1\,\mathrm{K}$, the estimated amount of tunnelling systems in amorphous
solids ranges between 10^{17} and 10^{18} per cm^3 [Ens05]. During polarisation echo experi-
ments where pulses of $100\,\mathrm{ns}$ duration are used, a total of approximately 4×10^{11} tunnelling
systems per cm^3 are resonantly excited [Fic13]. It is thus safe to say that every excited
tunnelling system, for further reference labelled as $\mathcal{A}$ system, is surrounded by many non-
excited, or $\mathcal{B}$, systems. If one of these neighbouring $\mathcal{B}$ systems undergoes a transition
between its energy levels due to a T_1 relaxation process i.e. absorption or emission of ther-
mal phonons, the elastic field around the $\mathcal{A}$ system is altered. Since external fields couple
to the diagonal elements of the Hamiltonian, the variation of the elastic field leads to a
variation of the asymmetry energy which in turn leads to a shift in the energy splitting of
the $\mathcal{A}$ system. As a result the eigenfrequency ω_{TS} is changed and the $\mathcal{A}$ system loses its
phase coherence with the other resonant $\mathcal{A}$ systems. Thus the T_2 relaxation mechanism
effectively has its origin in the interaction between tunnelling systems. The probability of
phonon-induced level transitions in $\mathcal{B}$ systems increases with time which is why the echo
amplitude decays for increasing pulse separations.

The theoretical description of the spectral diffusion is done with the help of the spin
formalism. In this context, the interaction between tunnelling systems can be seen as a
dipole-dipole interaction between spin i and spin j and, according to [BH77], is described
by the Hamiltonian

$$\hat{H}_{ij} = \sum_{ij} J_{ij} S_{\mathrm{z}}^i S_{\mathrm{z}}^j \tag{2.43}$$

where S_{z} denotes the spin operator with eigenvalues $\pm 1/2$. The coupling energy J_{ij} is
given by

$$J_{ij} = C_{ij} \left(\frac{\Delta}{E}\right)_i \left(\frac{\Delta}{E}\right)_j \frac{1}{r_{ij}^3} \tag{2.44}$$

with r_{ij} being the distance between spin i and spin j. The factor C_{ij} represents a material-
specific constant and depends on the tensor of deformation-potential coupling constants
at positions i and j. Allocating the index i to tunnelling systems $\mathcal{A}$ and j to tunnelling
systems $\mathcal{B}$, the effective Hamiltionian of an $\mathcal{A}$ tunnelling system can be written as

$$\hat{H}_{\mathrm{eff}}^i = E_{\mathrm{eff}}^i S_{\mathrm{z}}^i = E^i S_{\mathrm{z}}^i + \sum_{i \neq j} J_{ij} S_{\mathrm{z}}^i S_{\mathrm{z}}^j. \tag{2.45}$$

It is assumed that the relaxation time T_1 is larger than the measurement time such that
the tunnelling systems $\mathcal{A}$ do not return to their ground state via phonon emission. As a
result, S_{z}^i can be considered constant. Since the tunnelling systems $\mathcal{B}$ can change their
state through thermal phonon coupling, S_{z}^j and thus consequently E_{eff}^i are time-dependent.
In the following, an $\mathcal{A}$ tunnelling system with energy splitting $E = \hbar\omega_{\mathrm{TS}} \approx \hbar\omega_{\mathrm{EF}}$ at a time

$t = 0$ is considered. As time progresses, a random energy level transition of a neighbouring $\mathcal{B}$ system becomes more and more likely. The probability that the energy splitting of an $\mathcal{A}$ system changes from $E_{\text{eff}}^i = \hbar\omega_{\text{TS}}$ to $\hbar\omega$ at a time t is given by the diffusion kernel

$$D(\omega, t)\mathrm{d}\omega = \frac{1}{\pi} \frac{\Delta\omega(\mathrm{t})}{(\omega - \omega_{\text{TS}})^2 + \Delta\omega^2(\mathrm{t})} \tag{2.46}$$

which effectively describes a Lorentzian distribution. By accounting for all systems of both $\mathcal{A}$ and $\mathcal{B}$ type, the diffusion width, derived from the coupling energy, shows the following proportionality [BH77]

$$\Delta\omega(t) \propto \left\langle \left| \frac{\Delta}{E} \right| \right\rangle_{\mathcal{A}} \left\langle \left| \frac{\Delta}{E} \right| n_{\text{f}}(t) \right\rangle_{\mathcal{B}}. \tag{2.47}$$

The first factor $\langle |\frac{\Delta}{E}| \rangle_{\mathcal{A}}$ denotes the average of the sum over all $\mathcal{A}$ systems. Similarly, the second factor $\langle |\frac{\Delta}{E}| n_{\text{f}}(t) \rangle_{\mathcal{B}}$ is averaged over all $\mathcal{B}$ systems where r_{ij}^{-3} from the coupling energy (2.44) has been replaced by the density $n_{\text{f}}(t)$ of $\mathcal{B}$ systems which have undergone an odd number of energy state transitions during the time interval t. From the equation of the diffusion width it is also evident that tunnelling systems with a high asymmetry energy Δ interact more strongly with each other leading to a faster decoherence as compared to symmetric tunnelling systems.

Finally the contribution of the spectral diffusion for a two-pulse sequence towards the echo amplitude is given by [BH77]

$$W_{\text{S}}(t = 2\tau_{12}) = \left\langle \exp\left[\mathrm{i} \int_0^{\tau_{12}} \omega(\mathrm{t})\,\mathrm{d}\mathrm{t} - \mathrm{i} \int_{\tau_{12}}^{2\tau_{12}} \omega(\mathrm{t})\,\mathrm{d}\mathrm{t} \right] \right\rangle. \tag{2.48}$$

In fact, W_{S} includes the average over all $\mathcal{A}$ systems and over all the energy level transitions of their $\mathcal{B}$ system neighbours. In the short-time limit where the pulse separation τ_{12} is much shorter than the minimal relaxation time $T_{1,\text{min}}^{\text{B}}$ of the $\mathcal{B}$ systems, the contribution of the spectral diffusion can be written as [KA62]

$$W_{\text{S}}(t = 2\tau_{12}) = \mathrm{e}^{-q\,m(T)\tau_{12}^2} \tag{2.49}$$

describing thus a gaussian-shaped decay curve. The factor q is equal to Δ/E. According to [BH77] the parameter $m(T)$ shows the following temperature dependence

$$m(T) \propto T^4. \tag{2.50}$$

In the intermediate-time and in the long-time limit, the contribution of the spectral diffusion W_{S} takes on a different form. Said forms are derived in [Hu74] and will not be considered here.

The echo amplitude in the short-time limit $\tau_{12} \ll T_{1,\mathrm{min}}^{\mathrm{B}}$ can be calculated by taking into account the distribution function and integrating over q

$$A(t = 2\tau_{12}) \propto \int\limits_0^1 A_{\mathrm{echo}} P(q) W_{\mathrm{S}}(q, 2\tau_{12})\,\mathrm{d}q. \tag{2.51}$$

Here A_{echo} denotes the amplitude of the oscillating polarisation (2.39) of a single $\mathcal{A}$ tunnelling system, $P(q)$ is the distribution function from equation (2.18) and $W_{\mathrm{S}}(q, 2\tau_{12})$ represents the spectral diffusion contribution from equation (2.49).

By comparing both the T_1 and T_2 relaxation processes, it is evident that they influence the echo amplitude during different times. The spectral diffusion is the main reason for the decay of the echo amplitude at small pulse separation times. This decay, according to the theory laid out above, is gaussian. At larger pulse separation times, the T_1 relaxation process dominates. The corresponding echo decay is exponential. Taking into account both the T_1 and T_2 relaxation processes, the final echo amplitude at the time $t = 2\tau_{12}$ is given by

$$A(2\tau_{12}) \propto \int\limits_0^1 A_{\mathrm{echo}} P(q) W_{\mathrm{S}}(q, 2\tau_{12}) W_{\mathrm{R}}(q, 2\tau_{12})\,\mathrm{d}q \tag{2.52}$$

where $W_{\mathrm{R}}(q, 2\tau_{12})$ denotes the contribution from the T_1 relaxation (2.42). Inserting the corresponding equations into (2.52) yields

$$A(2\tau_{12}) = A_0 \tanh\left(\frac{E}{2k_{\mathrm{B}}T}\right) \int\limits_0^1 (1 - q^2)\,\mathrm{e}^{-T_{1,\mathrm{min}}^{-1}(1-q^2)2\tau_{12}}\,\mathrm{e}^{-qm\tau_{12}^2}\,\mathrm{d}q. \tag{2.53}$$

Here A_0 represents the echo amplitude that would theoretically be observed for $\tau_{12} = 0$ and $T = 0$. Additionally the occupation difference (2.15) has been included to ensure that only the tunnelling systems that are in the ground state prior to the application of the first pulse are considered.

2.5 Nuclear effects

The nuclear electric quadrupole effect is an additional effect that leads to a reduction of the echo amplitude and was already introduced in section 2.2.4. Said effect will briefly be described in this section.

Tunnelling systems involve several atoms whose nuclei may have a spin quantum number $I \geq 1$. The resulting orbital motion of the protons is related to a nuclear electric quadrupole moment. Additonally, the spatial charge distribution around the nucleus is non-isotropic which leads to an electric field gradient. The nuclear electric quadrupole moments can interact with the electric field gradient leading to a hyperfine splitting of

the two original energy levels into sublevels which causes additional decoherence effects [Wue02] [Wue04].
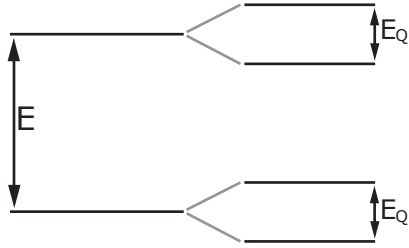
Figure 2.14: Sketch of the energy levels of a single tunnelling system of spin $I = 1$ with energy splitting E and quadrupole splitting E_Q. In zero magnetic field, the upper levels of both multiplets are degenerate.
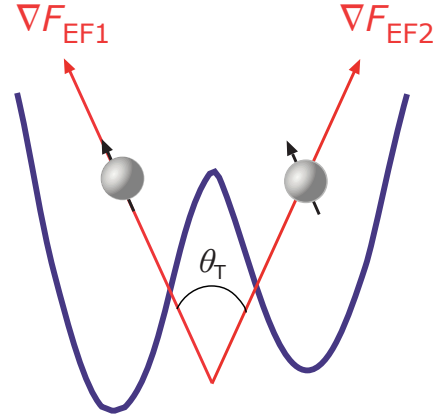
Figure 2.15: Schematic representation of a tunnelling particle carrying an nuclear electric quadrupole moment, indicated by the black arrows, in an antisymmetric double-well potential. The local electric field gradient $\nabla \boldsymbol{F}_{EF}$, represented by the red arrows, varies between the two wells by the rotation angle θ_T [Rue08].

In the following, the effect of such a hyperfine splitting on the echo amplitude is shown for the simple case of a two-level system with spin $I = 1$. Figure 2.14 shows the hyperfine splitting of the two original tunnelling states each into $m_I = -1, 0, +1$ sublevels. The sublevels with quantum number $m_I = \pm 1$ are degenerate, resulting in a four-level system. The hyperfine splitting E_Q of the upper and lower multiplet is much smaller than the energy splitting E. The corresponding tunnelling process of a tunnelling particle carrying a nuclear electric quadrupole moment in an antisymmetric double-well potential is portrayed in Figure 2.15. The tunnelling particle in the left well represents the situation prior to the application of the pulse sequence and hence prior to the tunnelling process. Its nuclear electric quadrupole moment is aligned along the orientation of the local electric field gradient. Their interaction leads to the aforementioned splitting of the ground state into the lower multiplet. If the hyperfine splitting is sufficiently small such that $E_Q \ll k_B T \ll E$, the tunnelling particle occupies either sublevel of the lower multiplet with equal probability. Due to the disorder of amorphous structures, reflected in the asymmetry energy, the orientation and magnitude of the electric field gradient varies between the two wells. Its orientation difference can be described by the rotation angle θ_T. The application of an electric pulse leads to the tunnelling motion of the particle from the left into the right well. Its nuclear electric quadrupole moment remains unchanged since the corresponding

nuclear relaxation times are much longer than the pulse duration. As a consequence, the nuclear electric quadrupole moment and the local electric field gradient are not aligned anymore and the tunnelling particle is forced to undergo a transition into a mixed state of the upper multiplet.

The additional energy states in the upper multiplet lead to additional possible temporal evolutions of the system. As a consequence, there is then also the possibility of additional destructive phase effects. The resulting decoherence leads to an oscillating decay of the echo amplitude with frequency $\omega_Q = E_Q/2\hbar$ known as 'quantum beating'.
In the case of two-pulse echoes, the echo amplitude for a tunnelling system with N atoms carrying nuclear electric quadrupole moments is given by [Par04]

$$A_{\text{echo}} \propto \left(\frac{\Delta_0}{E} \right)^4 \left[1 - A_{\text{mod}} \sin^4 \left(\frac{E_Q \tau_{12}}{2} \right) \right]^N \tag{2.54}$$

with modulation amplitude

$$A_{\text{mod}} = \frac{16}{3} \left(\frac{\Delta}{E} \sin \theta_T \right)^2 \tag{2.55}$$

Comparing equations (2.54) and (2.39), it is evident that the factor $(\frac{\Delta_0}{E})^4$ describes the maximal echo amplitude. Due to the nuclear quadrupole effect, the amplitude describes a oscillating beating of frequency $E_Q/2\hbar$ whilst decaying. The beating or modulation amplitude is given by A_{mod} and is proportional to Δ^2. This means that only antisymmetric tunnelling systems are influenced by the nuclear quadrupole effect. As seen in section 2.4, the antisymmetric tunnelling systems are also influenced by spectral diffusion. As a result, the nuclear quadrupole effect is expected to be only visible at small pulse separations and consequently the quantum beating decreases for increasing pulse separations. A more in-depth description as well as a successful experimental application of the nuclear quadrupole model can be found in [Baz08].

In multicomponent glasses there is the possibility of a variety of quadrupole splittings whose beating frequencies are superposed and are thus not distinguishable anymore. As a result, the decay of the echo amplitude, dominated by the highest beating frequency, is highest for small pulse separations. At larger pulse separations, where the quantum beating has already vanished, the echo amplitude is simply smaller compared to the maximal attainable amplitude in glasses without nuclear quadrupole moments.

The magnetic field dependence of the echo amplitude, as seen in Figure 2.9, is due to the interaction between the external magnetic field and the spins of the nuclei. For the same simple case with $I = 1$ described above, in a small magnetic field, the Zeeman interaction lifts the degeneracy of the $m_I = \pm 1$ sublevels leading to a Zeeman splitting of the energy levels. The energy splittings of the sublevels in the resulting six-level system

are then different from E_{Q} and hence the echo amplitude and the beating frequencies are changed. Increasing the magnetic field will lead to a greater Zeeman splitting until, at a very large magnetic field, the Zeeman splitting is much larger than the quadrupole splitting. As a consequence, transitions into a mixed state are suppressed and the system behaves like a pure two-level state without any quantum beating. The nuclear quadrupole effect then vanishes and the echo amplitude is maximal.

3. Experimental methods

In the framework of this thesis, the decay of the echo amplitude during two-pulse polarisation echo experiments was measured in two different dielectric glasses, BK7 and HY-1. This was done by measuring the echo amplitude for varying pulse separations τ_{12} at different constant temperatures. Since the formation of polarisation echoes is based on the coherent behaviour of the tunnelling systems, the glasses have to be measured in an environment that is kept at sufficiently low temperatures.
The BK7 glass was put into a nuclear demagnetisation refrigerator where it was possible to measure polarisation echoes at previously unattainable ultra low temperatures.
The HY-1 glass has been investigated in a ^{3}He/^{4}He-dilution refrigerator able to reach temperatures down to $8\,\mathrm{mK}$.
The general functioning of both the nuclear demagnetisation refrigerator and the ^{3}He/^{4}He-dilution refrigerator is well-known and can be looked up in [Ens05] and [Pob07] for example.

In the first section of this chapter the thermometry used in both cryostats is briefly described. The ensuing section illustrates the experimental setup by discussing the sample holders before showing how the glasses were integrated into the cryostats. In addition, to exemplify how two-pulse polarisation echoes can be generated and detected, the electronic setup is presented. Finally the chapter is concluded by a short analysis of the sample composition.

3.1   Thermometry

Since the decay of the polarisation echo amplitude was measured at different temperatures and over extended periods of times, it was mandatory to use appropriate thermometers which are not only able to determine the different low temperatures but are also able to help accurately maintain a fixed temperature over time. In general, one distinguishes between two categories of thermometers. Primary thermometers are able to determine the temperature of a system directly. This is possible if the temperature dependence of the system can be described by a fundamental physical law. Secondary thermometers can only be used to measure the temperature after they have been calibrated against other primary thermometers.

The secondary thermometer used in the ^{3}He/^{4}He-dilution cryostat to measure the temperature is a semiconducting carbon resistance thermometer [Wei95]. Semiconducting resistance thermometers are based on the temperature dependence of the ohmic resistance which increases for decreasing temperatures. The exact R-T behaviour varies from

thermometer to thermometer but is usually calibrated by the manufacturer. Due to its high resistance at low temperatures, the thermometer has to be probed by small currents in order to avoid significant heating of the resistor and thus an erroneous temperature read-out. As a consequence however, the temperature measurement lacks accuracy and fluctuates considerably.

The thermometer used in the nuclear demagnetisation refrigerator to measure temperatures down to $12\,\mathrm{mK}$ is a secondary resistance thermometer based on RuO_2 which has been calibrated against a superconducting fix-point device. The calibration curve as well as a detailed description of the RuO_2 thermometer can be found in [Rot13a].
Due to their high resistance at low temperatures, resistance thermometers are not suitable for measurements at ultra low temperatures. Hence, temperatures below $12\,\mathrm{mK}$ were measured by a noise thermometer. This type of thermometer is based on the Brownian motion of conduction electrons in a resistor. The resulting voltage fluctuation can be described by the Nyquist theorem and is directly related to the temperature. A more in-depth description of the functioning as well as the calibration of the noise thermometer used in the framework of this thesis can be found in [Rot13a] and [Rot13b].

3.2   Experimental setup

3.2.1   Resonators

The formation of polarisation echoes is achieved by exciting the glass samples via high-frequency electric pulses. This is realised by placing the samples in a reentrant cavity microwave resonator inside which electromagnetic standing waves can develop. These resonators are also called $\lambda/4$ resonators since their height is approximately equal to one fourth of the wavelength corresponding to their resonance frequency. Outside the resonator, the high-frequency pulses are carried by two coaxial cables.
As can be seen in Figure 3.1, the resonator consists of a hollow cylinder which is sealed off at the bottom and has a lid on top. The lid is connected to a rod leaving a gap of variable height above the bottom of the cavity if the resonator is closed. The sample is placed within this gap.
In the ^{3}He/^{4}He-dilution refrigerator, the resonator sits inside a superconducting coil made of niobium-titanium wire wound around a stainless steel cylinder with which a magnetic field can be generated. The body of the resonator sits on top of a column that is screwed to the experimental platform guaranteeing thus thermal contact between the resonator and the phonon bath of the cryostat whilst ensuring that the sample is positioned in the middle of the coil and thereby in a nearly homogeneous magnetic field. In the nuclear demagnetisation refrigerator, the resonator is placed inside a niobium shield instead of a coil in order to avoid being affected by external magnetic fields generated by the de-
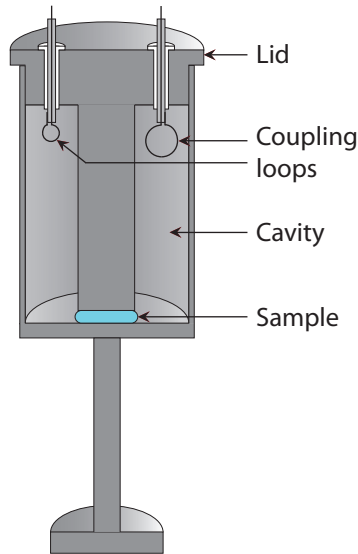
Figure 3.1: Sectional view of a reentrant cavity microwave resonator.
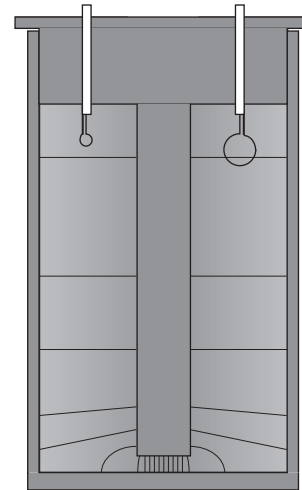
Figure 3.2: Sectional view of a reentrant cavity microwave resonator at a specific moment in time when the electric field energy is maximal. The thin lines represent the electric field lines.

magnetisation magnet. The coupling-in and coupling-out of the high-frequency signal is done inductively via two silvercoated copper loops. The loops are formed by connecting the internal conductor of a coaxial cable to its external conductor and can effectively be described as a coil with a single winding. The coaxial cables are entering the resonator through two teflon-isolated holes in the lid. The formation of an electromagnetic standing wave due to the alternating electric field passing through the loops can be exemplified by the radiation wave of a Hertzian dipole. The resulting electric field is maximal at the gap between the rod and the bottom of the cavity. The magnetic field is maximal in the vicinity of the lid while its field lines run radially around the rod. Due to the time evolution of the electromagnetic field, the total field energy inside the resonator oscillates between a moment of maximal magnetic field energy and minimal electric field energy respectively and a moment of minimal magnetic field energy and maximal electric field energy respectively. Figure 3.2 shows a distinct moment in time when the electric field, represented by the thin lines, is maximal. The denser the field lines, the stronger the electric field. In the gap between the rod and the bottom of the cavity, the electric field is strongest and most homogeneous which is why the samples are placed there. Due to the oscillation of the electromagnetic field energy, the reentrant cavity microwave resonator can be seen as an oscillating LC circuit where the cylinder walls, the rod and the loops act as the inductor while the gap acts as the capacitor.

The resonance curves of both resonators filled with either glass sample at a specific tem-
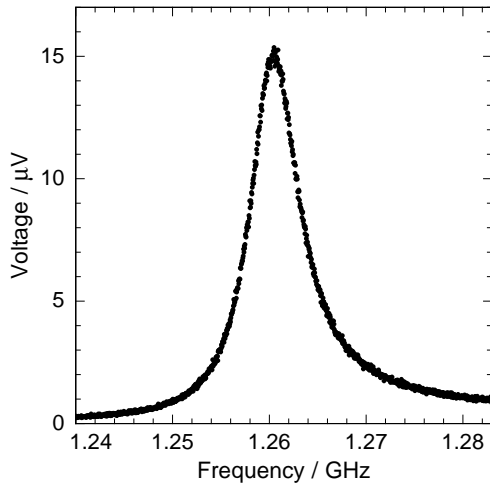
Figure 3.3: Resonance curve of the microwave resonator filled with BK7 at a temperature of 13.5 mK.
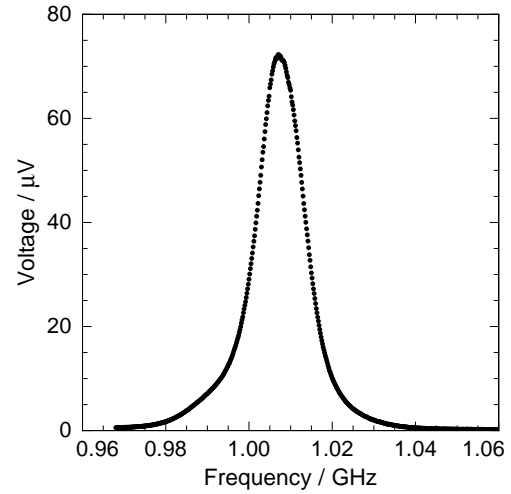
Figure 3.4: Resonance curve of the microwave resonator filled with HY-1 at a temperature of 10.1 mK.

perature are shown in Figure 3.3 and Figure 3.4. The resonance frequency of the resonator inside the nuclear demagnetisation refrigerator, containing the BK7 glass, was equal to roughly 1261 MHz at 13.5 mK while the resonance frequency of the resonator mounted inside the ^{3}He/^{4}He-dilution refrigerator, housing the HY-1 glass, was equal to roughly 1008 MHz at 10.1 mK. The resonance frequency depends on a lot of quantities such as the geometry of the resonator, the temperature or the dielectric properties of the sample itself. However, in the temperature range in which the measurements were taken, the resonance frequency was measured to be constant. Closely related to the resonance curve is the quality factor Q which describes how under-damped the resonator is. At the temperatures mentioned above, the quality factor of the resonator housing the BK7 glass was approximately 404 while the HY-1 filled resonator had a quality factor of roughly 139. The quality factor and the resonance frequency are related to the attack time which represents the time the resonator needs to start oscillating after an external perturbation. The attack time can be deduced from the quality factor and the resonance frequency via $\tau = Q/\omega_{\mathrm{R}}$. Inserting the values listed above, it becomes evident that the quality factor has to be as low as possible to ensure that the attack time is as short as possible since the high-frequency pulses used during dielectric polarisation echo measurements are only several hundred nanoseconds long.

The inductive coupling strength is determined by the area enclosed by the loops relative to the magnetic field lines and can be adjusted by either modifying their radii or by turning them with respect to the field lines. In the framework of this thesis, the coupling loops in both resonators were adjusted in the same way. The coupling-in loop was chosen to be smaller than the coupling-out loop in order to avoid an additional noise contribution

from the send-in branch while maximising the signal that was measured in the detection branch. Additionally, the coupling-in loop was turned by approximately 45° relative to the magnetic field lines.

The microwave resonator inside the ^{3}He/^{4}He-dilution refrigerator is made of copper whose thermal conductivity ensures good thermal contact between the sample and the experimental platform. Additionally, the resonator is gold-plated in order to avoid the formation of an oxide layer whose bad electrical conductivity would lead to unwanted heating. The hollow cylinder has a height of 70 mm and an inner radius of 18 mm. The conducting rod inside the cavity has a diameter of 8 mm. The column, connecting the main body of the resonator to the experimental platform, has a height of 29 mm.

The resonator inside the nuclear demagnetisation refrigerator is entirely made of silver. Its main body has a height of 54 mm and an internal diameter of 15 mm. The conducting rod has a radius of 6 mm while the column is 80 mm long.

3.2.2   Integration into the cryostats

The integration of the gold-plated copper resonator housing the HY-1 glass into the ^{3}He/^{4}He-dilution refrigerator is visualised in Figure 3.5 showing the important components of the cryostat and the echo experiment. The microwave resonator is mounted onto the experimental platform which is made of copper and is thermally connected to the mixing chamber where temperatures down to 8 mK can be reached. The high-frequency electric pulses are carried by two semi-rigid coaxial cables from the generation and detection unit at room temperature all the way down to the resonator inside a vacuum pot. Below the 1K pot, these semi-rigid cables are made of niobium which has a low thermal conductivity. Below a temperature of 9 K, niobium becomes superconducting and thus provides a desired low-noise signal transmission [Baz08]. The mixing chamber and experimental platform are surrounded by a double-walled and superconducting radiation shield made of copper and lead which protects them from thermal radiation and external magnetic fields. The shield is thermally coupled to the still. The vacuum pot resides in a super-isolated dewar filled with liquid ^{4}He.

Since the coaxial cables originate at room temperature, they have to be thermally intercepted along their way down to the resonator in order to avoid heating up the sample. This thermal interception is done in heat sinks which are made of gold-plated copper and are visually represented as yellow boxes in Figure 3.5. These heat sinks contain a sapphire substrate upon which two microstrip lines of niobium have been sputtered. The niobium lines carry the electrical signal of the inner conductor of the coaxial cables while the sapphire substrate, due to its excellent thermal conductivity, transports the heat to the heat sink. The heat sink itself is then screwed to various cold parts of the cryostat. The outer conductor of the coaxial cables is directly coupled to the heat sink. The microstrip lines are designed to have the same impedance as the coaxial cables, namely 50 Ω.

Coaxial
cables

Amplifier

4K flange

Heat sinks

1K pot

Attenuator

Still

Continuous
heat
exchanger

Vacuum
pot

Step heat
exchanger

Radiation
shield

Resonator

Mixing
chamber

Magnet

Experimental
platform

Carbon
thermo-
meter
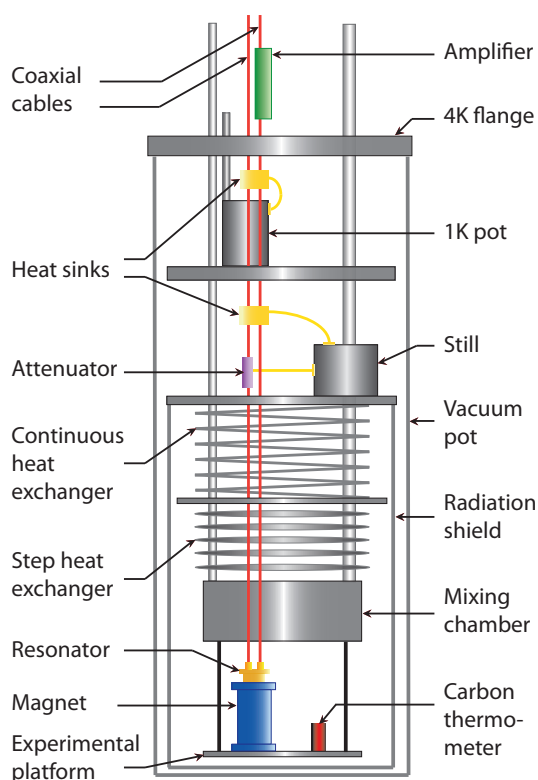
Figure 3.5: Schematic drawing of the echo experiment components inside the ^{3}He/^{4}He-dilution cryostat. The cryostat components are grey while the echo experiment components and the thermometer are colored.

Coming from the generation and detection units, the coaxial cables are fed into the vacuum pot after passing through the helium bath acting as the first cooling step. Inside the vacuum pot they are heat sunk two more times against the 1K pot and against the still at 0.7 K respectively. Below the still, the input signal passes through an 20 dB attenuator which ensures that the thermal noise is minimised upon reaching the resonator. The output signal, before exiting the cryostat, is passing through a 28 dB high-frequency amplifier at low temperatures in the helium bath leading to an amplified low-noise signal.

The carbon resistance thermometer is mounted onto the experimental platform. Since the thermometer, the mixing chamber and the resonator are well thermally connected, the measured temperature and the sample temperature are assumed to be identical.

The integration of the silver resonator housing the BK7 glass into the nuclear demagnetisation refrigerator is visualised in Figure 3.6. The refrigerator consists of a ^{3}He/^{4}He-dilution cryostat and two nuclear stages made of highly pure copper (6N). In the framework of this thesis, only the first nuclear stage was used and is connected to the mixing chamber of the dilution cryostat via a superconducting aluminum heat switch and three thin-walled aluminum oxide tubes. The resonator is mounted onto the experimental platform which is made of gold-plated copper and is located in a field-compensated area on top of the first nuclear stage. In order to compensate for the remaining magnetic field of 5 mT, the resonator is placed inside a niobium shield which is thermally coupled to the mixing chamber.
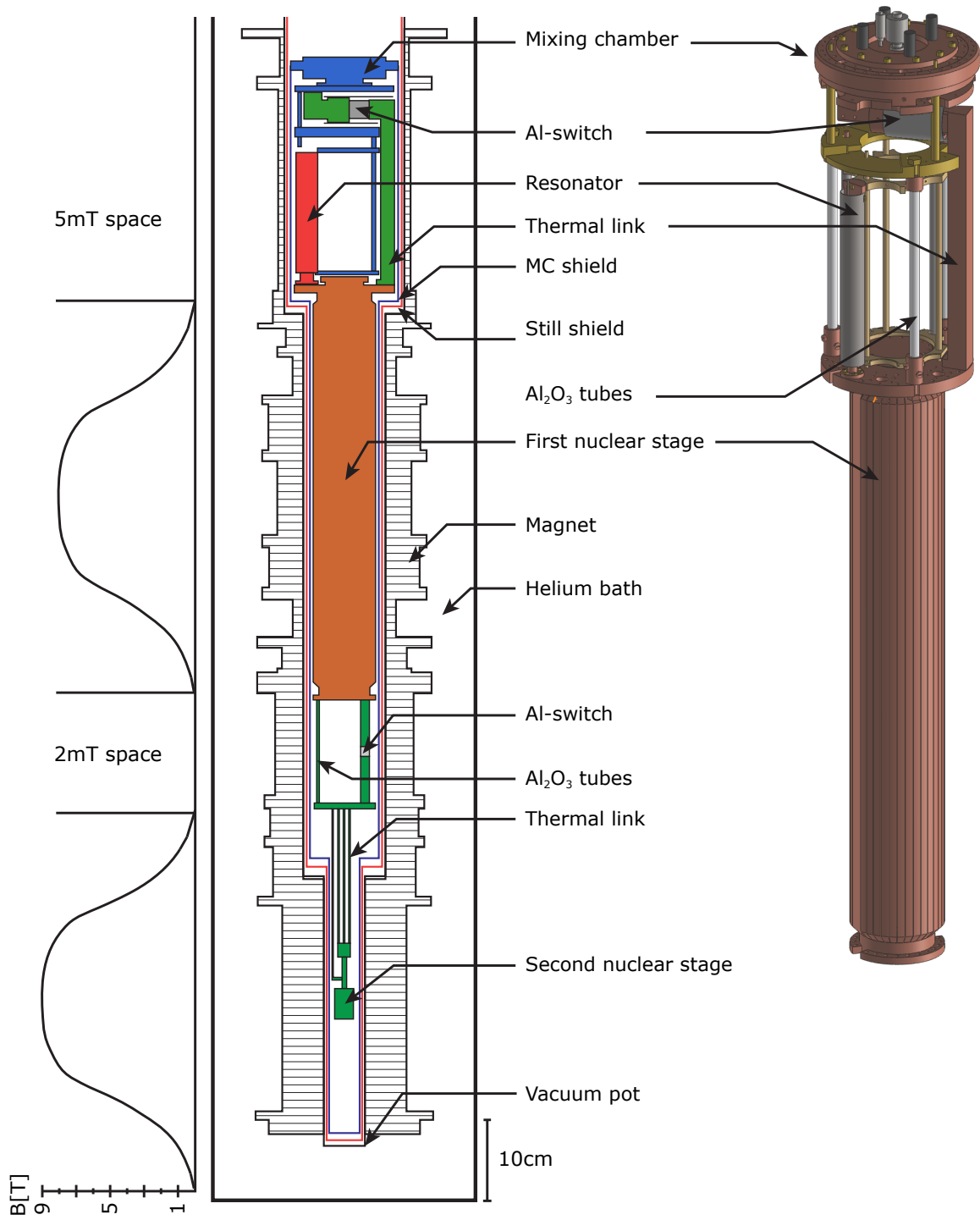
Figure 3.6: Sectional and three-dimensional view of the schematic setup of the nuclear demagnetisation cryostat [Rot13a]. Only the low temperature part of the cryostat is depicted. Above the mixing chamber the cryostat is roughly identical to a conventional ^{3}He/^{4}He-dilution cryostat. The RuOx and the noise thermometer are not depicted.

By exposing the superconducting aluminum switch to a magnetic field of $11\,\mathrm{mT}$, the switch is closed by becoming normalconducting and thus the nuclear stage is thermally coupled to the mixing chamber which is able to reach temperatures down to $12.5\,\mathrm{mK}$. By opening the aluminum heat switch and adiabatically demagnetising the nuclear stage, temperatures in the low microkelvin region are attainable. A more in-depth description of the nuclear stage as well as the heat switch used in the framework of this thesis can be found in [Glo88].

The experimental platform and nuclear stage reside in a radiation shield coupled to the mixing chamber which in turn resides in an additional radiation shield coupled to the still. The vacuum pot is surrounded by the demagnetisation magnet inside a ^{4}He bath and encapsulated from room temperature by a super-isolated dewar.

The high-frequency electric pulses are carried by two semi-rigid coaxial cables whose inner and outer conductors are made of cupronickel down to the 4K flange where they are thermally intercepted in a gold-plated copper heat sink. The inner conductor of the outgoing coaxial cable carrying the echo signal is silver-plated leading to a higher transmitted signal power. Below the 4K flange, the cupronickel coaxial cables are substituted by superconducting niobium-titanium semi-rigid coaxial cables. Their inner and outer conductors are heat sunk at the mixing chamber before entering the resonator. In contrast to the cable installation inside the ^{3}He/^{4}He-dilution cryostat in Figure 3.5, no attenuator or amplifier was inserted inside the nuclear demagnetisation cryostat.

When the nuclear stage is coupled to the rest of the the cryostat, the temperature is measured by the resistance thermometer based on $\mathrm{RuO_2}$ which is mounted onto the mixing chamber. Otherwise the temperature is measured by a noise thermometer consisting of two parts. One part is screwed to the mixing chamber while the other part is connected to the experimental platform. A more in-depth description of its installation is provided in [Rot13a]. Both thermometers are not depicted in Figure 3.6.

3.2.3 Electronic setup

Even though the sample resides inside the cryostat, the generation and detection units of the two-pulse polarisation echoes are operated at room temperatures. Figure 3.7 shows the circuit diagram of the electronic components of the echo setup for the HY-1 glass inside the ^{3}He/^{4}He-dilution refrigerator.

The signal generator (Rohde & Schwarz SMH) creates a continuous high-frequency signal with a defined amplitude and frequency. The frequency is set to be identical to the resonance frequency of the resonator. This main input signal is passing through a $3\,\mathrm{dB}$ power divider and is split into two parts of equal power. The right-hand branch signal is used as a reference signal and will be discussed further below. The signal of the left-hand branch reaches two consecutive switches which chop the continuous signal and thus generate two pulses. Rather than a single switch, a pair of switches is used in order to prevent the signal from leaking into the resonator inbetween the pulses. Consequently, if the switches

are open, the signal is attenuated by more than 80 dB [Sch12]. Furthermore, an attenuator of 5 dB is placed in between the switches in order to avoid the formation of standing waves. The durations, separation from one another and rate at which the switches open and close are controlled by a pulse generator (Stanford Research Systems DG535). Before entering the cryostat, the two high-frequency pulses pass a variable attenuator which is used to bring the signal down to an appropriate amplitude. The variable attenuator can be operated from 1 dB to 69 dB in steps of 1 dB.

Inside the cryostat, the signal passes through the in section 3.2.2 aforementioned 20 dB attenuator prior to entering the resonator. Before exiting the cryostat, the resulting signal passes through the 28 dB high-frequency amplifier at low temperatures (Kuhne electronics LNA-1020 A-COOL) mentioned in section 3.2.2. After returning to room temperature, the signal is fed into a circulator which prevents the backwards transmission of reflected
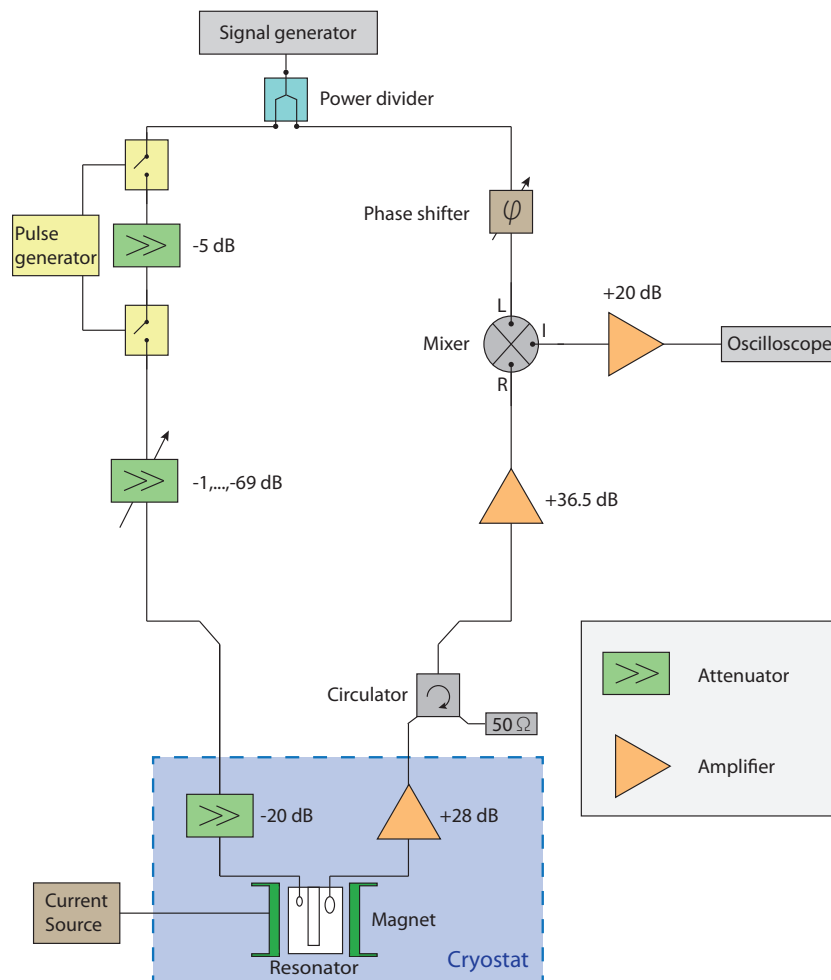
Figure 3.7: Circuit diagram of the electronic components needed to measure two-pulse polarisation echoes inside the ^{3}He/^{4}He-dilution cryostat. The components inside the blue box are located inside the cryostat whilst the other components operate at room temperature [Arc13].

waves into the cryostat by diverting them onto an attached $50\,\Omega$ resistor. Upon further amplification, the signal enters a mixer (MITeq DM0052LA2) where it is multiplied by the reference signal of the right-hand branch. This multiplication leads to the removal of the carrier frequency. Additionally, the multiplied signal is convoluted against the characteristic curve of the mixer leading to the removal of the negative values. The resulting signal consists thus only of the envelopes of the pulses, the free induction decay and the echo. A phase shifter is included in the right-hand branch to account for the phase difference between both signals and is set in such a way that the echo amplitude is maximal. The final signal is amplified one last time by a video amplifier before being fed into an oscilloscope where, after being averaged by a variable amount, the envelopes are displayed, digitised and sent to a computer.

A magnetic field can be generated inside the resonator by sending a current I, originating from a current source at room temperature (Keithley 2601A System SourceMeter), into the homemade superconducting magnet placed around the resonator. The strength of the magnetic field B is described by the linear relation

$$B = k \cdot I \qquad\qquad (3.1)$$

where $k = 0.229\,\text{T/A}$ is a magnet specific proportionality constant.

The circuitry used for the creation and detection of two-pulse polarisation echoes in the BK7 glass was similar to the one in Figure 3.7. As already mentioned in section 3.2.2, the circuitry inside the cryostat did not contain an attenuator or amplifier. A $20\,\text{dB}$ attenuator and a $28\,\text{dB}$ amplifier were thus inserted into the circuitry at room temperature as displayed in Figure 3.8.
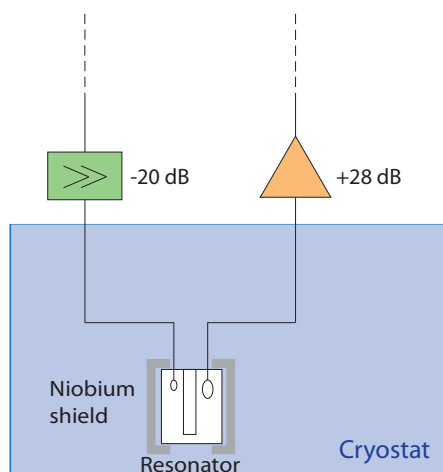
Figure 3.8: Circuit diagram of the electronic components needed to measure two-pulse polarisation echoes inside the nuclear demagnetisation cryostat. The components inside the blue box are located inside the cryostat whilst the other components operate at room temperature. Above the dashed lines the circuitry is identical to the one in Figure 3.7.

3.3   Glass samples

The sample contained in the silver resonator and investigated inside the nuclear demagneti-sation refrigerator was the optical glass BK7[1]. This glass is heavily based on borosilicate and is generally used to fabricate optical lenses. Its chemical composition is given in Table 3.1 where the molar percentages of the molecules are listed. The BK7 glass can be considered as rather well-known since its acoustic and dielectric properties have already extensively been investigated [Hun76] [Woh01]. Due to the relatively large dipole mo-

Ingredient	SiO_2	Na_2O	B_2O_3	K_2O	BaO	Al_2O_3
Amount	74.8%	10.1%	9.6%	4.7%	0.76%	0.03%

Table 3.1: Chemical composition of the BK7 sample measured inside the nuclear demagneti-sation refrigerator. The amount is expressed in molar percentages and has been determined by atomic emission spectroscopy at the Fraunhofer-Institut fuer Silikatforschung in Wuerzburg [Lud03].

ments of the tunnelling systems in BK7, it is possible to measure large echo amplitudes [Ens96]. As a consequence, two-pulse, three-pulse and rotary polarisation echoes have been measured at different low temperatures in a ^{3}He/^{4}He-dilution cryostat. Some of these measurements can be found in [Sch10], [Fas10], [Sch12] and [Fic13] for example. The glass sample completely fills the space between the rod and the bottom of the cavity inside the microwave resonator (as is displayed in Figure 3.1). Its thickness was measured to be 0.4 mm and it has been placed by using a small amount of silicone grease[2].

Ingredient	SiO_2	Na_2O	BaO	Ho_2O_3
Amount	68.2%	17.0%	8.1%	6.8%

Table 3.2: Chemical composition of the HY-1 sample measured inside the ^{3}He/^{4}He-dilution re-frigerator. The amount is expressed in molar percentages and has been determined by atomic emission spectroscopy by Varychev and Meyer at the Institut fuer Geowissenschaften in Heidel-berg. Further measurements by x-ray fluorescence analysis reveal an additional amount of less than 1% of both antimony and strontium (in molar percentages as well). It is assumed that the glass also contains B_2O_3 but this could not be measured.

The sample contained in the gold-plated copper resonator and investigated inside the ^{3}He/^{4}He-dilution refrigerator was the glass HY-1[3]. The glass contains a noticeable amount of holmium, a rare earth element, which carries a very large electric quadrupole moment. Moreover, holmium has the highest magnetic moment of any naturally occuring element. At ambient temperatures, holmium is paramagnetic but it becomes ferromagnetic at tem-peratures below 19 K [Jil98]. The chemical composition is provided in Table 3.2. In con-

---

[1]Manufactured by the company 'Schott AG' located in Mainz, Germany

[2]Baysilone paste by the company 'GE Bayer Silicones'

[3]Manufactured by the company 'Hoya Optics' located in Tokyo, Japan

trast to BK7, the HY-1 glass is relatively unknown. It is generally used in spectroscopy since the material presents a very narrow absorption line for blue light. The sample was under the form of a 12×12 mm square and had a thickness of 0.5 mm. As was the case for the BK7 glass, it was placed inside the resonator by using a small amount of silicone grease.

4. Data and discussion

In the framework of this thesis, two-pulse polarisation echoes were measured in the dielectric glasses BK7 and HY-1. In both experiments, the decay of the echo amplitude was measured by varying the pulse separation τ_{12} at several temperature steps. In BK7, the decay of the echo amplitude was measured at temperatures between $2.1\,\mathrm{mK}$ and $25\,\mathrm{mK}$ while in HY-1, the temperatures ranged from $8\,\mathrm{mK}$ to $15\,\mathrm{mK}$.

In the first section of this chapter is shown how the evaluation of the measured data was done as well as how statistical and systematic errors influence the measurement. The ensuing section presents the experimental results of the two-pulse polarisation echo experiments carried out on BK7 and is followed by a discussion about these results. Finally, the results of the measurements carried out on HY-1 are presented before the chapter is concluded by a discussion about the latter results.

4.1 Data evaluation

4.1.1 Evaluation of the echo amplitude

As described in section 3.2.3, the final signal, consisting of the envelopes of the pulses and the echo, is sent to an oscilloscope. The resulting displayed signal consists of 500 consecutive voltage readings which are separated by $10\,\mathrm{ns}$ in a $5\,\mu\mathrm{s}$ time window. To reduce the statistical noise to which every voltage reading is subjected, each reading can be averaged over a variable number of sweeps. The red curve in Figure 4.1 shows the echo signal for a pulse separation of $\tau_{12} = 5\,\mu\mathrm{s}$ at $15\,\mathrm{mK}$ in the glass HY-1, as displayed on the oscilloscope. The echo curve is not flat but is subject to an individual background and has an offset. The background can be measured separately by increasing the pulse separation such that the distance between the second pulse and the echo is sufficiently high whilst maintaining the time measurement window. This serves to send the echo far out of the time window such that only the unaffected background is displayed in the region where the echo-in-question would otherwise have arisen. Apart from that, the background measurement is taken under the same conditions as the raw echo measurement. The result of such a background measurement for an increased pulse separation of $\tau_{12} = 300\,\mu\mathrm{s}$ is represented by the black curve in Figure 4.1.

The appearence of a systematic non-flat background is due to two main reasons, one of which is the fact that the amplifiers in the detection branch of the electric circuit are overdriven by the pulses. Moreover, the two pulses passing through the circuitry and
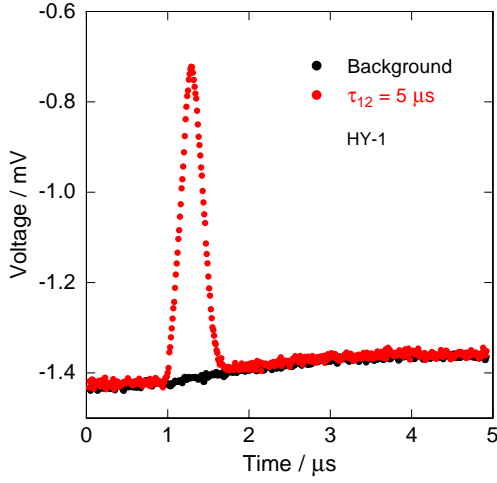
Figure 4.1: An echo curve and corresponding background measurement as displayed on the oscilloscope at a temperature of 15 mK for the HY-1 glass. The red curve corresponds to the echo at a pulse separation of $\tau_{12} = 5\,\mu$s. The black curve corresponds to a background measurement for $\tau_{12} = 300\,\mu$s.
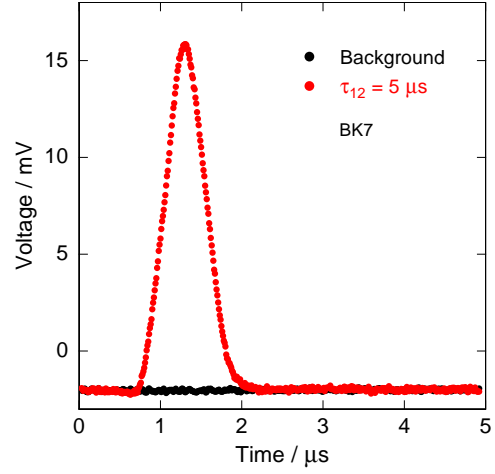
Figure 4.2: An echo curve and corresponding background measurement as displayed on the oscilloscope at a temperature of 15 mK for the BK7 glass. The red curve corresponds to the echo at a pulse separation of $\tau_{12} = 5\,\mu$s. The black curve corresponds to a background measurement for $\tau_{12} = 300\,\mu$s.

the cryostat are not perfectly rectangular, which is attributed to transient signals originating from the switches as well as residual oscillatory effects due to the fact that the resonator needs a certain amount of time to equilibrate following the application of the high-frequency pulses. The non-rectangular pulses affect the region right after the point at which perfectly rectangular pulses would have ended. As a result, the form of the echo is significantly changed for small pulse separations. Furthermore, for a particular temperature and pulse separation, the background has shown to vary over the course of several hours. A more in-depth description and analysis of the systematic background in two-pulse polarisation echo experiments conducted inside the ^{3}He/^{4}He-dilution cryostat can be found in [Arc13].

For comparison, Figure 4.2 shows the echo and background curve for the BK7 glass inside the nuclear demagnetisation refrigerator. The two curves were averaged by the same amount of sweeps as for the HY-1 glass, while the power of the high-frequency signal and thus the amplitude of the pulses was different. Therefore, the signal height of the echo in both glasses cannot be compared while a comparison of the statistical noise of the underlying background is still possible. For HY-1, the statistical noise which is imposed on the background curve is characterised by typical voltage variations of roughly 0.01 mV. For BK7, the background curve is subject to noise of roughly 0.2 mV voltage variations, which is 20 times larger than the statistical variation of the background curve for the HY-1 glass,

making a systematic voltage variation impossible to discern. This can be explained by the fact that the signal exiting the resonator inside the ^{3}He/^{4}He-dilution cryostat is passing through a low-noise amplifier residing in the helium bath while the respective signal inside the nuclear demagnetisation cryostat is only amplified at room temperature (see section 3.2.3). Although both amplifiers are characterised by the same gain, the low-noise amplifier inside the helium bath causes a significant reduction of the noise leading to a superior signal-to-noise ratio. The lack of an equivalent amplifier inside the nuclear demagnetisation cryostat leads to a large noise contribution and is thus the reason why it is impossible to discern a non-flat background curve for the BK7 glass.

The decay of the echo amplitude is investigated by ultimately measuring an appropriate quantity that sufficiently describes the echo signal strength. A straightforward choice of such a quantity would be the highest voltage reading of the echo signal. However, since the signal-to-noise ratio decreases for increasing temperatures and pulse separations (due to the signal becoming weaker), this quantity is affected too much by statistical noise. A less noise-sensitive, and thus better, quantity is the so-called integrated echo amplitude (IEA) that is calculated by summing over all the voltage readings in a specific time interval and multiplying the result by the time separation of two readings. As a consequence, the IEA is directly proportional to the amplitude of the echo signal. The accuracy of the IEA relies upon the assumption that the echo curve lies flat on the $0\,\text{V}$ x-axis. As discussed before in this section, this is not the case, as the echo curve is subject to a systematic background and an offset. Thus, in order to calculate the IEA, the echo curve has to be corrected.

This is achieved, in a first step, by subsequently measuring the background and the corresponding raw echo and then pointwise subtracting the background from the raw echo. The result is an echo signal lying on a flat curve. Since the background may vary over the course of several hours, measurements with large sweep numbers have to be divided in blocks of alternating background and raw echo measurements of smaller but equal sweep numbers. Since the measured background is also subject to noise, the pointwise subtraction leads to a higher overall noise which cannot be avoided.

In a second step, the offset is rectified. This is done by subtracting the average value of a number of points outside the echo region from all the points of the curve. The offset correction does not introduce additional noise.

In this context, Figure 4.3 shows the corrected echo curve for three different pulse separations at a temperature of $15\,\text{mK}$ in BK7. The integrated echo amplitude is entirely calculated in region (1) which shows the actual echo. The flat region (2) is used for the determination of the offset as well as the statistical noise.

Increasing the temperature or pulse separation leads to a smaller echo signal. As an example, Figure 4.4 shows the corrected echo curve for $\tau_{12} = 130\,\mu\text{s}$ at $15\,\text{mK}$ in BK7. The echo is subject to high noise but is still easily discernible. By increasing the number
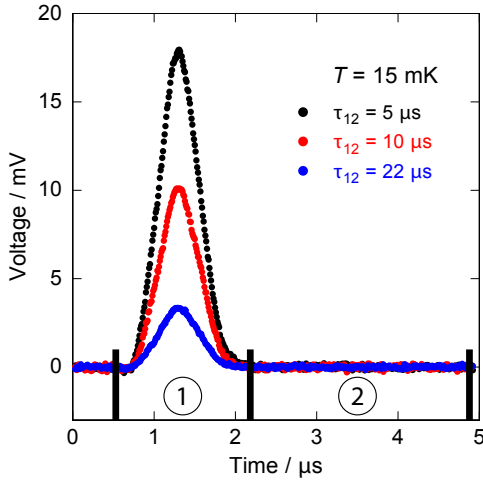
Figure 4.3: Corrected echo curves for three different pulse separations τ_{12} at $15\,\mathrm{mK}$ in BK7. The actual echo lies in region (1) while the flat curve in region (2) is used for the offset correction as well as the determination of the statistical noise.
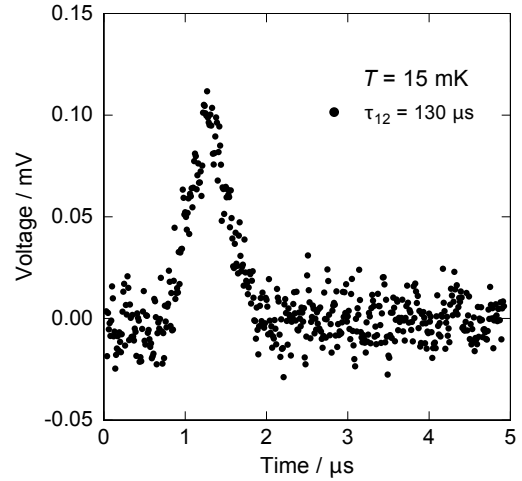
Figure 4.4: Corrected echo curve for a pulse separation of $130\,\mu\mathrm{s}$ at a temperature of $15\,\mathrm{mK}$ in BK7. The curve has been averaged over 1.4×10^5 single measurements.

of sweeps, it is possible to reduce the statistical noise. An useful quantity in that regard is the signal-to-noise ratio which is discussed in more detail in the following section.

4.1.2   Error analysis

As already mentioned, the voltage signal can be affected by both statistical and systematic errors. The statistical errors are identified as the electronic noise originating from sources in the electronic setup and lead to a gaussian distribution of the voltage readings. In the case of the electronic setups used in the framework of this thesis (see section 3.2.3), the dominant statistical noise can be identified as white noise stemming from the various amplifiers.

In order to measure echo signals at higher temperatures and large pulse separations, the electronic noise has to be minimised as much as possible such that a clear echo can still be identified. This is done by increasing the amount of times the measurements are averaged. If the measured voltage readings are indeed statistically distributed, their standard deviation should be proportional to $\frac{1}{\sqrt{N}}$, where N is the number of sweeps. In recent measurements, it has been proven that this is the case [Sch12] [Fic13] [Arc13] [Ahr13]. Figure 4.5 shows the standard deviation σ of the data points from region (2) of the raw echo curve, i.e. without an additional noise contribution due to the background correction, plotted against the number of sweeps N for the HY-1 glass. The graph shows that
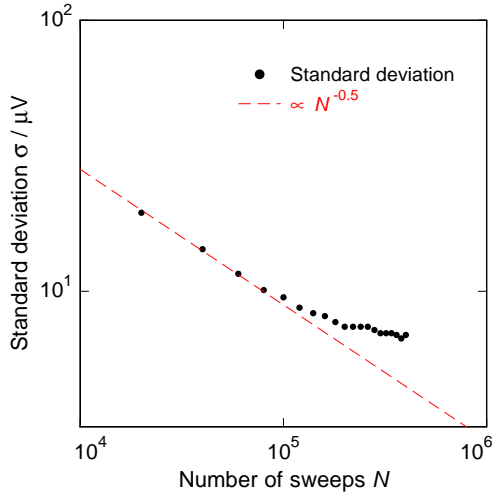
Figure 4.5: Standard deviation σ of the data points from region (2) of the raw echo curve for $\tau_{12} = 20\,\mu s$ at $8\,mK$ plotted against the number of sweeps in HY-1. The dashed red line represents the $\frac{1}{\sqrt{N}}$-proportionality.
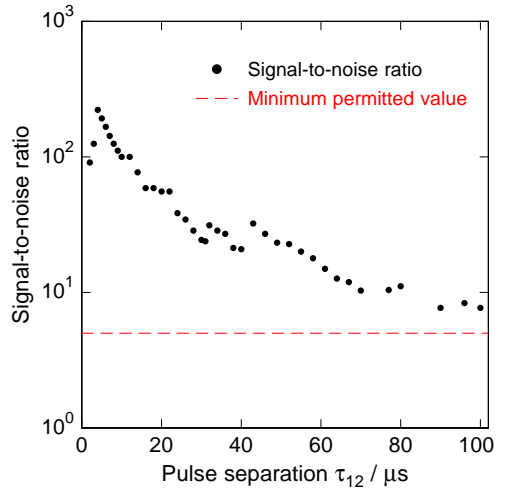
Figure 4.6: Signal-to-noise ratio of the corrected echo curve for all pulse separations in BK7 at $20\,mK$. The dashed red line represents the minimum permitted value for the signal-to-noise ratio.

the standard deviation follows the aforementioned proportionality for low N but seems to become almost constant for higher N. This means that the statistical noise cannot be reduced any further and is ultimately limited by systematic noise.

In order to decide whether the echo signal in region (1) is still substantially larger than the statistical noise in region (2), the aforementioned signal-to-noise ratio is calculated. This is done by dividing the maximum height of the echo in region (1) by the standard deviation of all the data points in region (2). The number of sweeps is chosen such that the signal-to-noise ratio is above an arbitrarily set minimum permitted value of 5. As an example, Figure 4.6 shows the signal-to-noise ratio for all pulse separations at $20\,mK$ in BK7. At small pulse separations, the echo signal is strong such that a small number of sweeps is sufficient to reach an appropriate signal-to-noise ratio. At higher pulse separations however, due to increased phase-destroying processes, the echo signal is getting smaller and a higher number of sweeps is necessary. Depending on the temperature and pulse separation, the number of sweeps could range from 1000 to 400 000 or more during the measurement. Choosing the appropriate number of sweeps depends on several factors such as the time available for a measurement or the fact that, as already shown in Figure 4.5, the statistical noise would eventually not decrease any further. A more in-depth discussion about the statistical noise in the ^{3}He/^{4}He-dilution cryostat is provided in [Fic13].

Beside the statistical errors, the measurements are also affected by systematic errors which can be divided into two groups: either an error leads to a non-statistical shift of the echo

amplitude or the error directly influences the tunnelling systems and thus their phase-coherent behaviour, leading to a different decay of the echo amplitude.

Systematic errors belonging to the former group have already been encountered in Figure 4.5 and are the reason why the statistical noise is not reduced upon further averaging. These systematic errors could be caused by additional electronic signals inside the high-frequency circuit such as transients that are reflected inside the cables and thus form standing waves which are superposed on the echo signal. Furthermore, the stability of the integrated echo amplitude signal can be investigated over the course of several hours to see if there are any systematic drifts due the electronic components of the circuitry. As is shown in [Baz08] and [Rue08], the integrated echo amplitude measured inside the ^{3}He/^{4}He-dilution refrigerator presents a slight upward drift over several hours. This drift could be explained by the sinking helium level inside the cryostat. Since the coaxial cables carrying the high-frequency signals are passing through a helium bath before entering the vacuum pot, a sinking helium level leads to a temperature change of the cables and thus alters the degree of damping which affects the detected signal. Additionally, the low-noise frequency amplifier at low temperatures is also located inside the helium bath and probably displays a similar dependence on the current helium level as well. Inside the nuclear demagnetisation cryostat, a similar but weaker drift has been observed. This is indicated in Figure 4.7 showing the normalised integrated echo amplitude at a constant pulse separation of $10\,\mu$s at a temperature of $4\,$mK over the course of approximately 15 hours. The red line serves as a guide to the eye and helps identifying an upward drift of the integrated echo amplitude.
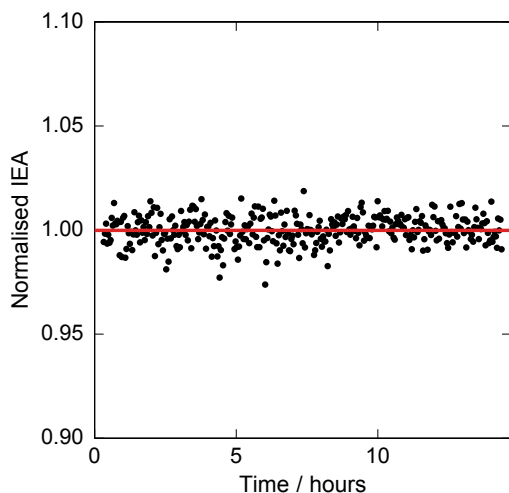
Figure 4.7: Normalised integrated echo amplitude at a pulse separation of $10\,\mu$s at a temperature of $4\,$mK in BK7 plotted against time. The red line serves as a guide to the eye.

Systematic errors altering the phase-coherent behaviour of the tunnelling systems and thus reducing the echo amplitude originate mostly from external sources. Mechanical vibrations, which can be identified as one of these sources, can deform the glass sample itself, leading to a change of the potentials and finally to a shift of the energy splitting. As a result, some resonant tunnelling systems are losing their phase coherence and are not able

to contribute towards the echo, leading to a smaller total echo amplitude. As is derived in [Fic07], deformations of the sample dimension of the order of 10^{-3} Å are sufficient to cause an observable reduction of the echo amplitude. Mechanical vibrations can be induced by the pumps or loud noises in the vicinity of the cryostat and are coupling to the resonator housing the glass samples via the framework of the cryostat itself. Moreover, vibrations can also be generated inside the cryostat through the 1K pot while it is filling with helium. Inside the ^{3}He/^{4}He-dilution refrigerator, the filling process occurs every 3 hours and lasts roughly 30 minutes. During the filling process, the computer programm is automatically paused and restarts 5 minutes after the filling is done. However, if the oscilloscope is currently averaging over a certain number of measurements while the filling process starts, the measurement will not be paused. This is why sweeps are generally taken in smaller blocks so that only a small data set is affected by the 1K pot vibrations and can be removed from the final data. Inside the nuclear demagnetisation cryostat, the 1K pot is constantly filling with helium so that the resonator is permanently subject to mechanical vibrations. While these vibrations may reduce the echo amplitude, the decay of the echo curve does not seem to be overly affected (see section 4.2.2). In general, to check the stability of the measurement, reference echoes are included among the normal echo measurements at regular time intervals. These reference echoes consist of echoes with a small but constant pulse separation such that their measurement time is short and does not significantly extend the total length of the measurement. By comparing the integrated echo amplitude of these reference echoes, it is possible to see if any external effects may have influenced the measurement at a specific time. The affected data set can then be identified and excluded should it be necessary.

The echo amplitude is also affected by small temperature fluctuations inside the cryostat. The temperature of the experimental platform is regulated by a PID controller which ensures that the temperature is being kept constant and compensates for any undesired heating effects. Despite the excellent thermal coupling of the resonator, the thermometer and the mixing chamber, it may still be possible, due to their spatial separation for example, that the temperature measured by the thermometer does not correspond to the temperature of the mixing chamber or of the resonator. These discrepancies are assumed to be very small but should not be neglected.

Furthermore, the temperature of the glass sample may be raised during the application of the high-frequency electric field pulses. This depends on the length and the power of the pulses as well as on the repetition rate of the switches. These heating effects will be discussed in detail in the following section.

4.1.3   Length and amplitude of the pulses

By sending in pulses that are too long, it is possible deform the shape of the echo. This action is called 'overwinding' since the pseudospin vectors of the tunnelling systems inside the Bloch sphere are rotated by more than 90° and 180° respectively. Figure 4.8 shows the corrected echo curves for two pulse sequences of different duration at a fixed pulse separation of 80 μs and a temperature of 2.9 mK in BK7. The black curve corresponds to the echo measured after applying a $\frac{\pi}{2}$-pulse of 225 ns length and a π-pulse of 450 ns length while the red curve corresponds to the echo measured after applying a $\frac{\pi}{2}$-pulse of 300 ns length and a π-pulse of 600 ns length. By comparing the shape of both echoes, it is evident that the echo measured after applying the 300-600 ns pulse sequence is deformed while the echo measured after applying the 225-450 ns pulse sequence retains its regular, triangular form. Since overwinding the pseudospin vectors is an undesirable action, it is necessary to determine the ideal duration of the pulse sequence during which the glass sample is exposed to the electric field prior to measuring any echo decay curves. This is achieved by measuring the echo curve at a fixed pulse separation for varying pulse lengths and subsequently investigating for which duration of the pulse sequence the IEA is maximal while the echo is still maintaining its triangular shape.

Long pulses not only can cause a deformation of the echo shape due to overwinding but
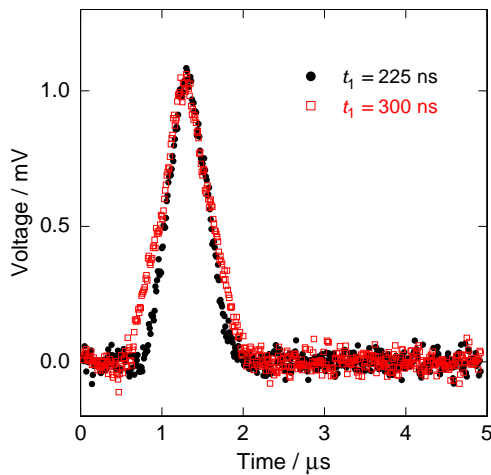
Figure 4.8: Corrected echo curves for two pulse sequences of different duration at a pulse separation of 80 μs and a temperature of 2.9 mK in BK7. The quantity t_1 corresponds to the length of the first pulse. The second pulse was of double duration.
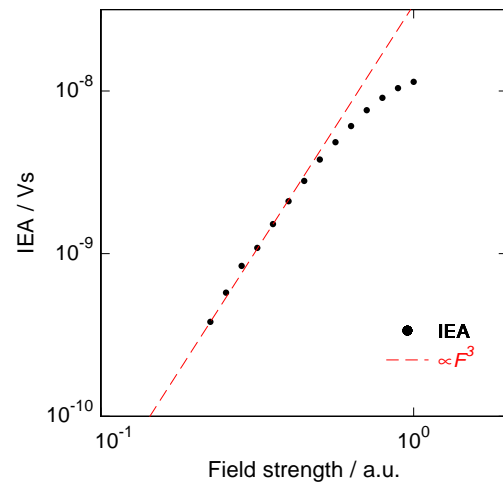
Figure 4.9: IEA of HY-1 plotted against the field strength at a pulse separation of 2 μs and a temperature of 15 mK. The rightmost data point corresponds to the IEA at original signal power. The leftmost data point corresponds to the IEA where the power of the pulses has been attenuated by 13 dB.

also because the glass sample is longer exposed to the high-frequency electric field and thus may be heated up. Additionally, instead of using pulse sequences that are too long, the glass sample can also be heated up by sending in pulses of too much power. As a consequence, the form of the echo can also be deformed. This can be avoided by attenuating the sent-in signal power at room temperature. In section 2.3.2, it was derived that the amplitude of two-pulse polarisation echoes is proportional to the third power of the Rabi frequency $A_{\mathrm{echo}} \propto \Omega_{\mathrm{R}}^3$ (see equation (2.39)). Since the Rabi frequency itself is linearly proportional to the strength of the electric field (see equation (2.30)), it is expected that the integrated echo amplitude varies with the third power of the field strength. As an example, Figure 4.9 shows the IEA of the HY-1 glass at a pulse separation of $2\,\mu$s and a temperature of $15\,$mK plotted against the field strength. This was achieved by measuring the echo curve for different pulse power levels by operating the variable attenuator (see Figure 3.7) from $0\,$dB (rightmost data point in Figure 4.9) to $13\,$dB (leftmost data point in Figure 4.9) in steps of $1\,$dB. From the graph it is clear that the echo amplitude does not follow the F^3-proportionality, as indicated by the dashed red line, in HY-1 if the signal is not attenuated at room temperature. By bringing down the power of the pulses to an appropriate level, it is possible to end up in the regime where the echo amplitude is described by the theory. In the situation described above, the IEA started to follow the F^3-proportionality after an attenuation of at least $6\,$dB.

Similarly to the determination of the duration of the pulse sequence, the determination of the appropriate power level should be done prior to any echo decay measurement. Even though the attenuation of the signal prevents the sample from heating up, the measured IEA is ultimately smaller and the echo will not be detectable for as large pulse separations as would be the case if the signal were not attenuated.

The trigger rate of the switches is the repetition rate of the pulse sequence and defines the rate at which the switches are opened and closed and thus the frequency at which the pulses are sent into the cryostat. Since the tunnelling sytems inside the glass samples need a certain amount of time to re-equilibrate after an external perturbation, the trigger rate has to be adjusted depending on the temperature and the nature of the glass sample itself. In the framework of this thesis, the trigger rate that was used ranged between $10\,$Hz and $50\,$Hz. For comparison, for two-pulse polarisation echoes measured in the AlBaSi glass, trigger rates up to $120\,$Hz were used. Using a repetition rate of the pulse sequence that is too high will also heat up the glass sample. This will be shown in the following section.

4.2   Experimental results of BK7

4.2.1   Echo decay curves

Two-pulse polarisation echo experiments on BK7 inside the nuclear demagnetisation refrigerator yielded the echo decay curves shown in Figure 4.10, where the integrated echo amplitudes are plotted in single-log representation as a function of pulse separation τ_{12} at eight different temperatures ranging from 2.1 mK to 25 mK. Every data point corresponds to the IEA determined from a corrected echo curve where the signal-to-noise ratio was kept above the minimum permitted value. During the experiment, it was found that the absolute values of the IEA would vary prior to and after the filling of helium into the dewar since, as was mentioned in section 4.1.2, the helium level affects the attenuation of the electrical components residing in the helium bath. Generally, in order to account for these variations, overlapping data points are measured which provide scaling factors that can then be used to compare and merge the data sets between different filling sessions. In the case of the polarisation echo measurements on BK7, each IEA decay curve was measured within a single session between the fillings which means the data set did not need to be merged. Additionally, the slight drift in the IEA over time, as shown in Figure 4.7, did not lead to a perceptible change of the IEA in the decay curves represented in Figure 4.10. In the case of the polarisation echo measurements on the glass HY-1, presented in section 4.4, the measurement of a whole decay curve could last up to one week and the data sets had to be merged.

The decay curves all start at a minimum pulse separation of $\tau_{12} = 2\,\mu$s. With the electronic setup used in the framework of this thesis, lower pulse separations could not be reached due to the finite width of the pulses. As a result, the initial level of coherence directly after the first pulse could not be observed. The largest measured pulse separation of the decay curves ranged from $\tau_{12} = 77\,\mu$s at 25 mK to $\tau_{12} = 175\,\mu$s at 2.1 mK.

The decay curves show that the IEA decreases for increasing pulse separations. This is due to the greater amount of time during which the system is exposed to decoherence effects which reduce the size of the echo. Additionally, the decay rate of the IEAs is observed to decrease for increasing pulse separations. This is due to the influence of spectral diffusion on antisymmetric tunnelling systems which results in them quickly losing their phase coherence. For increasing pulse separations, more and more antisymmetric tunnelling systems lose their phase coherence until hardly any are left and only the remaining symmetric tunnelling systems, which are not influenced by spectral diffusion, contribute to the echo. The decay of the IEAs is dictated by two relaxation mechanisms and is governed by equation (2.53). At small pulse separations, where spectral diffusion causes the antisymmetric tunnelling systems to lose their phase coherence, the decay of the IEAs is gaussian. At larger pulse separations, where the remaining symmetric tunnelling systems
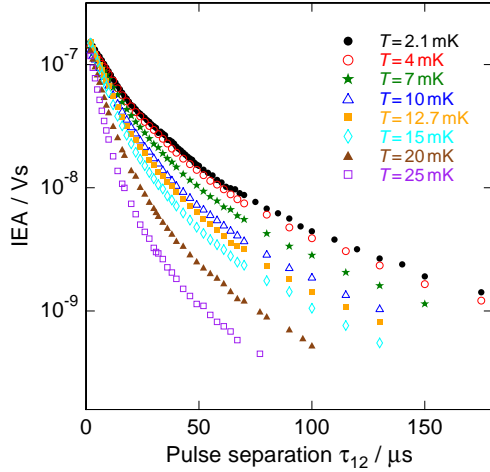
Figure 4.10: Echo decay curves measured during two-pulse polarisation echo experiments on BK7 at eight different temperatures. The IEA is plotted logarithmically versus the pulse separation τ_{12}.
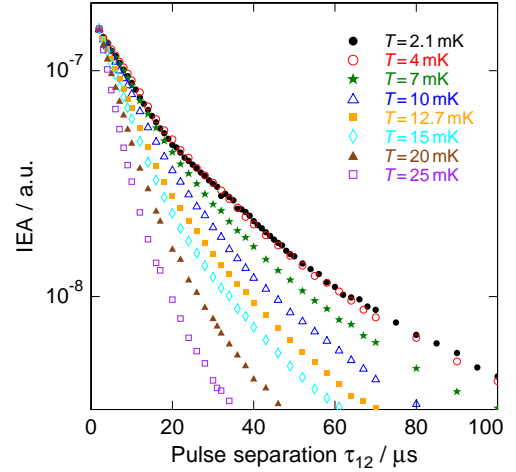
Figure 4.11: Same echo decay curves as in Figure 4.10 plotted at smaller pulse separations. Each curve was scaled such that its IEA at a pulse separation of $\tau_{12} = 2\,\mu s$ was identical, leading to the same starting point for all curves.

can lose their phase coherence via one-phonon processes, the decay is exponential. Furthermore, the initial decay rate of the curves increases for increasing temperatures. This can be attributed to the temperature dependence of the T_2 relaxation rates, induced by spectral diffusion and governed by equations (2.49) and (2.50), of the antisymmetric tunnelling systems. The T^4-dependence of the T_2 relaxation rate effectively causes the initial decay rate to increase for increasing temperatures. The temperature dependence of the decay rate is smaller at large pulse separations since, by then, the majority of the antisymmetric tunnelling systems have lost their phase coherence and the temperature dependence of the decay curve is dictated by the T_1 relaxation rate which predicts a linear temperature dependence according to equation (2.41). Thus the decay rate is expected to increase with increasing temperatures faster at small than at large pulse separations. However, the decay curves at temperatures below $12.7\,\mathrm{mK}$ hint at the fact that the decay rate becomes constant for large pulse separations. In previous two-pulse polarisation echo experiments on BK7 [Fas10] and AlBaSi [Arc13], where the IEA decay curves were measured for larger pulse separations, the same observation was made. In [Fic13] the T_1 relaxation mechanism in BK7 is investigated via three-pulse polarisation echo experiments. The results of these experiments also show a temperature independence of the decay rate at larger pulse separations. Further analysis yielded that this temperature independence is not caused by external perturbations to the system such as vibrations or electromagnetic noise, but rather by an unknown intrinsic property of the tunnelling systems not yet considered by theory.

Even though the decay curves in Figure 4.10 do not start at the same absolute value of the IEA, they appear to converge to a similar value for a pulse separation approaching $\tau_{12} = 0\,\mu s$. In previous polarisation echo experiments, decay curves at higher temperatures have been measured and reveal that above $25\,mK$, the curves do not exhibit this convergence to a similar value at zero pulse separation [Fic13]. This discrepancy has been attributed to the thermal population difference described by equation (2.15) which accounts for the fact that at higher temperatures, fewer tunnelling systems are in the groundstate prior to the application of the pulses. Thus there are fewer resonantly excited tunnelling systems that are able to contribute to the echo. For the temperatures used in the framework of this thesis, this effect could not be observed. However, the absolute values of the IEA between the different temperatures below $20\,mK$ show some minor discrepancies at the smallest pulse separation of $\tau_{12} = 2\,\mu s$. These discrepancies are in the order of magnitude of the IEA varying over time due to systematic errors and thus probably do not have any physical interpretation.

In Figure 4.11 the decay curves are displayed at shorter pulse separations. Additionally, each curve has been multiplied by a numerical factor such that their IEAs for a fixed pulse separation of $\tau_{12} = 2\,\mu s$ are identical. This serves to better compare the initial rate of decay, due to spectral diffusion, as well as observe a peculiarity in the decay of the curves at the two lowest temperatures of $2.1\,mK$ and $4\,mK$. Qualitatively, these two curves behave the same way and differ from the rest by exhibiting a 'bump' between $20\,\mu s$ and $60\,\mu s$. The same behaviour has been found at similar temperatures such as $2.6\,mK$ and $2.8\,mK$ (see section 4.2.3).

4.2.2 Comparison with previous data

In 2010, two-pulse polarisation echo experiments were carried out on BK7 inside the ^{3}He/^{4}He-dilution refrigerator (presented in chapter 3) by Paul Fassl in the framework of his Bachelor thesis [Fas10]. Since the measurements on BK7 presented in this report have been carried out in the nuclear demagnetisation refrigerator, it is interesting to compare the results of both experiments. This is done in Figure 4.12 where the echo decay curves measured during both experiments are shown. The curves represented by the full symbols correspond to the measurements carried out in 2010 while the curves represented by the open symbols correspond to the measurements carried out in 2014. In order to qualitatively compare the results from both experiments, the echo decay curves measured in 2014 were multiplied by a numerical factor such that the IEAs at pulse separation $\tau_{12} = 58\,\mu s$ are identical. The comparison reveals that the decay of the echo curves at both temperatures are qualitatively identical between the two experiments. However, there are some discrepancies at small pulse separations that could be explained by the different backgrounds underlying the echo curves as is shown in section 4.1.1. These backgrounds affect the echoes close to the second pulse the most and thus seem to be the main reason why
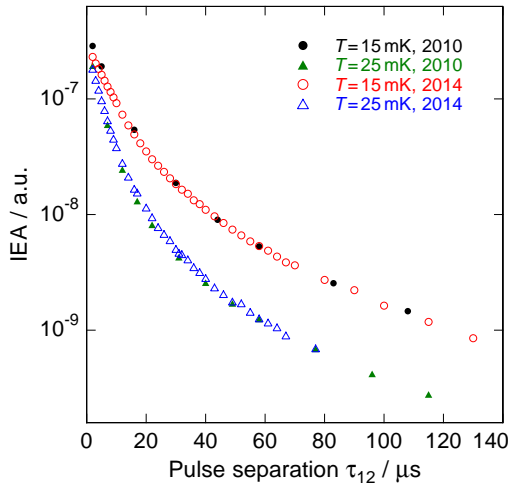
Figure 4.12: Comparison of two sets of echo decay curves measured four years apart in two different experimental setups and cryostats. The curves plotted in full symbols were measured in 2010 inside the ^{3}He/^{4}He-dilution refrigerator [Fas10] while the curves plotted in open symbols are from 2014 and were measured inside the nuclear demagnetisation refrigerator. The only common temperatures at which both experiments were carried out were 15 mK and 25 mK.

the IEAs differ at small pulse separations between the curves measured in 2010 and 2014. This is also the reason why the scaling of both sets of curves was done at the relatively large pulse separation of 58 μs.

Nonetheless, given that both experiments were carried out in two different cryostats and experimental setups, the agreement between both is excellent and shows that no cryostat or setup specific systematic errors influence the data.

The echo decay curves inside the ^{3}He/^{4}He-dilution refrigerator in 2010 were measured up to much larger pulse separations than inside the nuclear demagnetisation cryostat in 2014. The inability to measure echoes at much larger pulse separations in the latter cryostat is mainly due to the lack of a low-noise high-frequency amplifier at low temperatures in the circuitry.

4.2.3 Heat input at very low temperatures

In Figure 4.10 it can be seen that the echo decay curves at the two lowest temperatures of 2.1 mK and 4 mK qualitatively behave the same. Additionally, Figure 4.11 shows that their IEAs are almost identical, even at larger pulse separations. This is rather suprising given that the IEAs between the other decay curves differ significantly. Further measurements, one of which was carried out at 2.6 mK, reveal that the decay curves seem to be identical at the lowest temperatures measured during the experiment.

In this context, Figure 4.13 shows echo decay curves which were measured at four different temperatures and with the same trigger rate of 15 Hz. The echo decay curve measured at 7 mK was included to better compare the three curves at lower temperatures to one at higher temperatures. While the echo decay curve measured at 4 mK shows a slightly faster decay at pulse separations below 100 μs, the curves measured at 2.1 mK and 2.6 mK are identical. Given that the results presented in this chapter are the results from the very
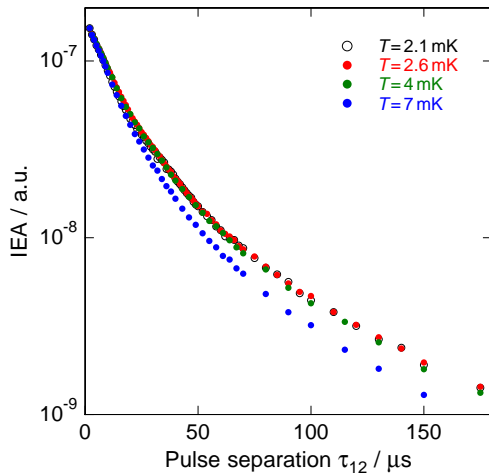
Figure 4.13: Echo decay curves of BK7 measured at four different temperatures. All four curves were measured with a trigger rate of 15 Hz. The curves at 2.6 mK, 4 mK and 7 mK were scaled so that all three curves have an identical IEA at a pulse separation of 2 μs.
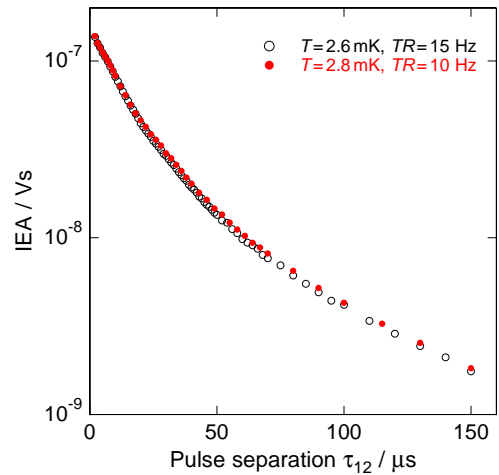
Figure 4.14: Echo decay curves of BK7 measured at two different temperatures and with different trigger rates. Both curves did not need to be scaled since they already shared the same IEA at a pulse separation of 2 μs.

first two-pulse polarisation echo measurements carried out at temperatures below 7 mK on BK7 at the time of writing, the observation that echo decay curves measured at different temperatures behave exactly the same has never been made before.

Further measurements have revealed that the identical behaviour of the echo decay curves at temperatures of 2.6 mK and 2.1 mK could be explained by the assumption that the glass is not getting colder because the power that is sent in is too high. This assumption is supported by the measurements shown in Figure 4.14 where the already discussed echo decay curve at 2.6 mK is compared to a decay curve at 2.8 mK that has been measured with a lower trigger rate of 10 Hz. A qualitative comparison shows that the decay rate of the echo curve at 2.8 mK is lower than at 2.6 mK, which contradicts the temperature dependence of spectral diffusion. It can thus be concluded that the temperature of the glass sample measured with a trigger rate of 15 Hz is in reality higher than the temperature of the glass sample measured with a trigger rate of 10 Hz. This is due to the fact that the glass is more frequently exposed to the pulses if the repetition rate of the pulse sequence is higher as well as the fact that the tunnelling systems do not have enough time to re-equilibrate.

The power sent into the resonator can be quantified. For the two-pulse polarisation echo measurements carried out inside the nuclear demagnetisation refrigerator, the total power of the pulses after passing through the 20 dB attenuator at room temperature, as shown in

Figure 3.8, amounted to $81\,\mu$W. The first pulse had a duration of $230\,$ns while the second pulse was of double duration, namely $460\,$ns. Using a trigger rate of $15\,$Hz, the power the glass is exposed to would the signal be constantly sent into the resonator amounts to $85\,$pW. Similarly, for a trigger rate of $10\,$Hz, the total power is equal to $57\,$pW. According to [Rot13a], in a previous run, the experimental platform inside the nuclear demagnetisation refrigerator was able to stay below $100\,\mu$K for several days while suffering a parasitic heat input of $\dot{Q}_{\mathrm{par}} = 310\,$pW. In contrast, the total power sent in by the pulses is thus smaller than this parasitic heat input by one order of magnitude.

The echo decay curves measured at temperatures below $7\,$mK and shown in Figures 4.13 and 4.14 exhibit the same 'bump' that was already mentioned in section 4.2.1. The measurements of the echo decay curve at $2.1\,$mK and the ones at $2.6\,$mK and $2.8\,$mK were carried out more than a month apart which means that the bump is reproducible.

4.3   BK7 Discussion

The echo decay curves measured in BK7 inside the adiabatic demagnetisation refrigerator were the first to be measured in a dielectric multicomponent glass below a temperature of $7\,$mK at the time of writing. The results of these measurements, as can be seen in Figures 4.11 and 4.13 for example, reveal that the echo decay curves at these previously unattainable low temperatures exhibit a 'bump' between pulse separations of approximately $20\,\mu$s and $60\,\mu$s.
Comparison with echo decay curves measured in 2010 by Paul Fassl in the framework of his Bachelor thesis [Fas10] shows that the data is not influenced by cryostat or setup specific systematic errors. Measurements with different input powers have revealed that heating effects lead to a uniform reduction of the echo amplitude across almost the whole range of pulse separations. As a result, it can be concluded that the bump is neither due to systematic errors nor due to heating effects but seems to be a property of the glass itself.

The shape of the bump is such that it could be part of a quantum beating superposed on the echo decay curve. This quantum beating would then be the result of nuclear effects as described in section 2.5. However, as can be seen from previous measurements on BK7 [Fas10] [Sch12] [Fic13], a quantum beating has never been observed at higher temperatures. This thus begs the questions as to why such a beating would only manifest itself at lower temperatures. This could be further investigated by measuring the echo decay curve to larger pulse separations in order to see whether a similar second bump would appear.

Another explanation would be that the bump is due to a phase transition inside the glass below a certain temperature. As was reported by Strehlow et al., at a critical temperature of $T_{\mathrm{c}} = 5.84\,$mK, experiments investigating the dielectric function in AlBaSi hinted at a

possible phase transition [Str98]. It is assumed that, at this phase transition, the uncorrelated and incoherent tunnelling motion of the individual tunnelling systems crosses over to a coherent and collective motion. According to Strehlow, similar results have been found in BK7. This new coherent and collective motion may show up in the occurrence of the bump.

4.4 Experimental results of HY-1

4.4.1 Echo decay curves

The echo decay curves of the glass HY-1 acquired during two-pulse polarisation echo measurements at two different temperatures of $8\,\text{mK}$ and $15\,\text{mK}$ are shown in Figure 4.15. As was mentioned in section 4.2.1, the absolute values of the IEA would vary prior to and after the filling of helium into the dewar. Since the measurement of a single echo decay curve could last up to a whole week, the measurement of the IEA at a pulse separation of $\tau_{12} = 4\,\mu\text{s}$ was included in every measurement and served to provide a scaling factor with which the different data sets could be combined into an entire decay curve. The pulse separation of $\tau_{12} = 4\,\mu\text{s}$ was chosen because it provided a strong echo signal and did not need to be averaged over a large number of times and thus it did not substantially extend the overall measurement time. As was the case for the echo decay curves measured in the nuclear demagnetisation cryostat, the drift of the IEA over time, as reported in section 4.1.2, did not noticeably influence the absolute values of the IEA in Figure 4.15.

Both decay curves start at almost the same IEA value before decaying at different rates due to phase-destroying effects to a minimal IEA at a pulse separation of $\tau_{12} = 25\,\mu\text{s}$. Echoes beyond this pulse separation could barely be recognised and presented signal-to-noise ratios that were too low and could not be ameliorated by increasing the number
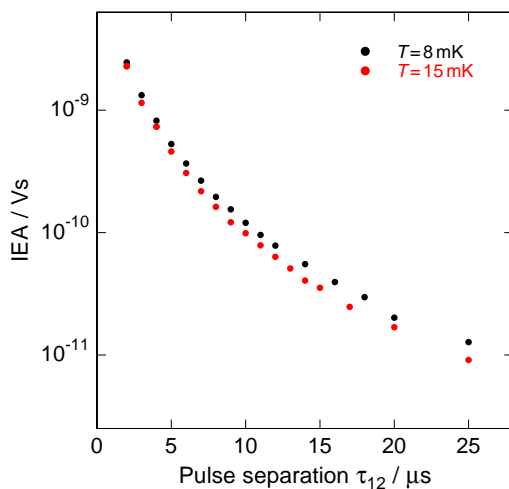
Figure 4.15: Echo decay curves measured during two-pulse polarisation echo experiments on HY-1 at two different temperatures. The IEA is plotted logarithmically as a function of pulse separation τ_{12}.

of sweeps. This is due to underlying systematic noise as was shown in Figure 4.5. The smallest detectable echo presented an absolute IEA very similar to the ones measured in BK7 [Fic13] and AlBaSi [Arc13].

The difference in the initial decay rate between the two curves is due to the temperature dependence of spectral diffusion, as was already described in section 4.2.1. By comparing the echo decay curves in HY-1 and BK7, i.e. Figures 4.15 and 4.10, it becomes evident that the IEAs of the echo decay curves in HY-1 are smaller than the ones in BK7 by two orders of magnitude over the whole range of pulse separations. Additionally, at the corresponding temperatures, the IEA of HY-1 is reduced by two orders of magnitude over a pulse separation interval of $23\,\mu$s while the IEA of BK7 is reduced by the same amount over a bigger pulse separation interval of approximately $150\,\mu$s. Thus the decay rate is much higher in HY-1 than in BK7.

4.4.2   Comparison with other glasses

The difference in the decay rate can better be seen in a direct comparison of the echo decay curves between different glasses. In this context, Figure 4.16 shows the echo decay curves measured in BK7, AlBaSi and HY-1 at pulse separations up to $140\,\mu$s and a temperature of $15\,$mK. Similarly, Figure 4.17 shows the echo decay curves in AlBaSi and HY-1 in the same pulse separation interval at a temperature of $8\,$mK. No echo decay curve in BK7 at
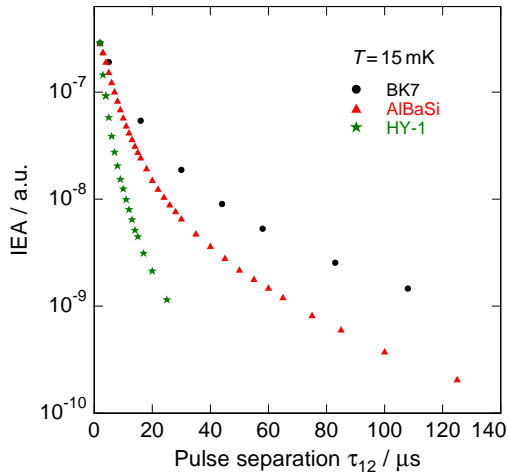
Figure 4.16: Scaled echo decay curves measured in three different multicomponent glasses at a temperature of $15\,$mK. The echo decay curve of BK7 was measured in 2010 [Fas10] while the one for AlBaSi was measured in 2013 [Arc13].
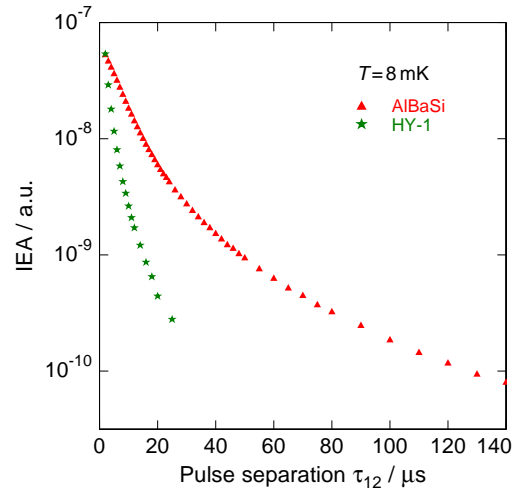
Figure 4.17: Scaled echo decay curves measured in two different multicomponent glasses at a temperature of $8\,$mK. The echo decay curve of AlBaSi was measured in 2013 [Arc13].

the same temperature was available. While the BK7 data are from 2010 [Fas10] and the AlBaSi data from 2013 [Arc13], all measurements were carried out in the same ^{3}He/^{4}He-dilution refrigerator. To better compare the decay rate, the curves were scaled such that their IEAs at a pulse separation of $\tau_{12} = 2\,\mu\text{s}$ were identical.

The qualitative comparison shows that the decay rate in HY-1 is indeed much higher than in the other two multicomponent glasses. This is the consequence of an additional, not yet considered phase destroying effect that occurs in the HY-1 glass. This ultimately leads to a reduction of the echo amplitude and a much faster phase decoherence of the tunnelling systems than in the other glasses. As will be discussed in section 4.5 this additional phase decoherence is assumed to be most likely due to nuclear quadrupole effects.

4.4.3 Measurement in a magnetic field

In addition to measuring the echo decay curves at different temperatures, first measurements of the echo decay curve were conducted inside a magnetic field of 229 mT. The result of this measurement, along with the echo decay curve taken without an applied magnetic field at the same temperature of 15 mK, can be seen in Figure 4.18.

The result of the experiment shows that the application of a magnetic field leads to a much higher echo amplitude. In fact, at the smallest pulse separation of $\tau_{12} = 2\,\mu\text{s}$, the
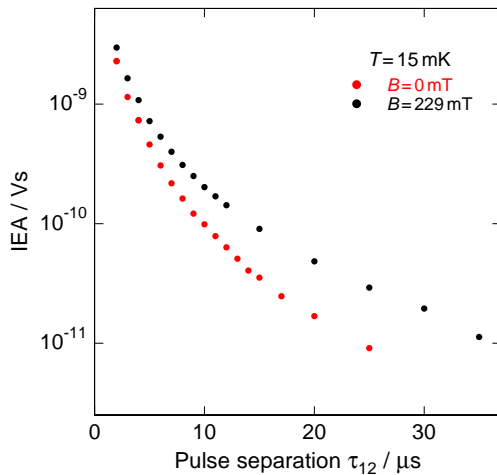
Figure 4.18: Echo decay curves measured in two-pulse polarisation echo experiments on HY-1 with and without application of a magnetic field of 229 mT at a temperature of 15 mK.
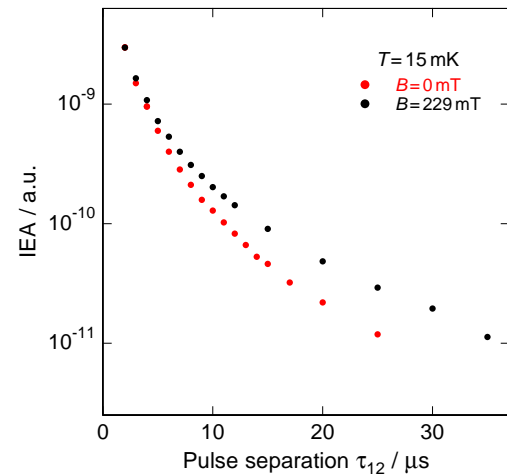
Figure 4.19: Scaled echo decay curves measured in two-pulse polarisation echo experiments on HY-1 with and without application of a magnetic field of 229 mT. The red curve was scaled such that its IEA at a pulse separation of $\tau_{12} = 2\,\mu\text{s}$ was identical to the one of the black curve.

IEA of the decay curve measured inside the magnetic field is 77% larger than the IEA of the decay measured without a magnetic field. This discrepancy is more than 10 times larger than a deviation caused by systematic errors and thus has to originate from the properties of the glass itself. Moreover, it can be excluded that heating effects are the cause for the difference between the two echo decay curves since, on one hand, heating would cause a reduction of the echo amplitude and, on the other hand, ample time was provided after the magnet was ramped so that the sample could thermalise appropriately before the measurement was started.

In addition to having an overall higher echo amplitude across the whole range of pulse separations, the echo decay curve measured inside the magnetic field also presents a much smaller decay rate. This can better be seen in Figure 4.19 where the curves were scaled onto each other at a pulse separation of $\tau_{12} = 2\,\mu$s and thus allow for a better qualitative comparison.

Due to the fact that the echo amplitude was larger and did not decay as fast as without applied magnetic field, it was possible to measure the echo decay curve to larger pulse separations. At even larger pulse separations, given the progression of the echo decay curves, one expects the IEA without magnetic field to be noticeably smaller than the ones measured in the magnetic field.

4.5 HY-1 Discussion

Two-pulse polarisation echo measurements carried out on HY-1 have shown that the echo amplitude is much smaller than in other glasses. In fact, compared to BK7, the echo amplitude in HY-1 was measured to be two orders of magnitude smaller. Additionally, the decay rate at small pulse separations has been found to be much higher in HY-1 than in other multicomponent glasses such as BK7 or AlBaSi. It can thus be concluded that there seems to exist an additional phase destroying effect in HY-1, not considered by spectral diffusion, that leads to a reduction of the echo amplitude as well as to a much faster decay of the echo amplitude as a function of pulse separation.

As was noted in section 3.3, HY-1 contains a noticeable amount of holmium which carries a very large nuclear electric quadrupole moment. As was described in section 2.5, the interaction between nuclear electric quadrupole moments and local electric field gradients can lead to a hyperfine splitting of the two energy levels considered in the standard tunnelling model and thus to additional phase destructive interference effects due to the possibility of additional level transitions. According to theory, this leads to a quantum beating which is superposed on the echo decay curve. However, since the hyperfine splitting energies are broadly distributed in a multicomponent glass, only an average reduction of the echo amplitude but no distinctive beating, as can be seen in amorphous deuterated glycerol [Nag04] [Baz08], is observable. According to equations (2.54) and (2.55), the nuclear quadrupole

effect is most important at small pulse separations where antisymmetric tunnelling systems have not yet lost their phase coherence due to spectral diffusion but are still contributing to the echo. The strong nuclear electric quadrupole moments in holmium may be the reason why the echo amplitude is much smaller in HY-1 than in other multicomponent glasses.

For increasing pulse separations, more and more antisymmetric tunnelling systems lose their phase coherence due to spectral diffusion and thus the nuclear quadrupole effect diminishes in strength. The application of a magnetic field should suppress the transitions between the hyperfine levels due to the Zeeman splitting, leading to effective two-level systems, and thus cancel the effects of phase destructive interference. At larger pulse separations, where only symmetric tunnelling systems contribute to the echo, the progression of the echo decay curve inside the magnetic field is expected to follow the one without magnetic field. As a result of the application of a magnetic field, a higher echo amplitude a small pulse separations should be observable.

From Figure 4.18, it can be seen that the echo amplitude measured in a magnetic field is indeed higher at small pulse separations. In fact, at the smallest pulse separation of $\tau_{12} = 2\,\mu$s, the IEA of the decay curve measured inside the magnetic field is 77% larger than the IEA of the decay curve measured without an applied magnetic field. This increase in the amplitude is most likely due to the partial cancellation of the phase destructive interference effects, caused by the interaction between nuclear electric quadrupole moments and the local electric field gradients, in a magnetic field. Additionally, for increasing pulse separations, the decay rate of the IEA is reduced. This cannot be entirely explained by the previously mentioned nuclear effect and is also in direct contrast to the result of a similar experiment conducted on AlBaSi [Ahr13]. In this experiment, it was found that the IEA was up to 15% larger at small pulse separations if a magnetic field was applied, but was again reduced to its original value at larger pulse separations. This latter behaviour is predicted by the nuclear quadrupole effect while the behaviour at larger pulse separations in a magnetic field in HY-1 is not accounted for by this theory.

Thus it can be assumed that the small echo amplitude and the fast phase decoherence of the tunnelling systems in HY-1 is partly due to nuclear effects and partly due to an additional decoherence effect that also couples to the magnetic field. In fact, as was mentioned in section 3.3, holmium carries the largest magnetic moment of any naturally occuring element. It may thus be possible that relaxation mechanisms that are closely related to this magnetic moment lead to decoherence effects by directly influencing the tunnelling systems, as in spectral diffusion, resulting thus in a reduction of the echo amplitude and a much faster decay rate. An applied magnetic field may then couple to these magnetic moments and subsequently increase their relaxation times which ultimately results in a smaller decay rate of the echo amplitude.

Further low-frequency dielectric and acoustic experiments carried out on HY-1 have also revealed additional relaxation mechanisms. The results of these measurements strongly hint to the fact that these relaxation mechanisms may indeed be due to nuclear effects [Luc] [Hem].

5. Summary and conclusion

In the framework of this thesis, two-pulse polarisation echo experiments were carried out on the borosilicate glass BK7 inside a nuclear demagnetisation refrigerator at temperatures down to 2.1 mK in order to investigate a possible phase transition.

The relaxation mechanisms in BK7 have already extensively been investigated in the temperature range between 7 mK and 70 mK [Fas10] [Sch12] [Fic13] thus creating a basis upon which can be built by extending the measurements to ultra low temperatures. Low-frequency dielectric constant measurements carried out on the aluminoborosilicate glass AlBaSi have provided evidence for a possible phase transition below a critical temperature of $T_c = 5.84$ mK [Str98]. A very similar observation was made in other multicomponent glasses such as BK7 thus motivating measuring at temperatures below T_c in order to investigate if the phase transition would have any effect on the polarisation echoes.

Furthermore, it is assumed that another relaxation mechanism, due to nuclear effects, is leading to an additional phase decoherence of the tunnelling systems in glasses [Wue02] [Wue04]. These effects have already been observed in echo experiments on partially deuterated glycerol [Nag04] [Baz08]. In order to investigate nuclear effects in multicomponent glasses, two-pulse polarisation experiments have been conducted on HY-1, a glass containing a noticeable amount of holmium which carries a very large nuclear electric quadrupole moment, with and without application of a magnetic field of 229 mT.

In the two-pulse polarisation echo experiments carried out on BK7 at temperatures below and including 4 mK, a peculiar 'bump' in the echo decay curve has been observed between pulse separations of approximately 20 μs and 60 μs. Through comparisons with echo decay curves measured in 2010 at higher temperatures inside a ^{3}He/^{4}He-dilution cryostat [Fas10], it was found that no cryostat or setup specific systematic errors influenced the measurement. Furthermore, through comparisons with echo decay curves measured at different power levels, it was also found that heating effects do not cause the observable bump but uniformly reduce the echo amplitude across almost the whole range of pulse separations. It was thus concluded that the bump seems to stem from an intrinsic property of the glass itself. As an explanation, the phase transition observed by Strehlow et al. was suggested. However, the bump is such that a quantum beating superposed on the echo decay curve cannot be categorically denied.

Additional measurements are thus necessary to shed light on this matter. Two-pulse polarisation echo experiments in a magnetic field, for example, could determine whether the bump is due to nuclear effects or not. Including a high-frequency amplifier at low temperatures into the circuitry inside the vacuum pot of the nuclear demagnetisation refrigerator

would make it possible to increase the signal-to-noise ratio and measure echoes to larger pulse separations in order to see if other bumps can be detected. This amplifier would also help in detecting an echo signal even if the sent-in power were greatly reduced. As a consequence, it would be possible to measure echoes at even lower temperatures. In this context, using a coplanar resonator and a thinner glass sample would ameliorate the thermal coupling and work towards futher reducing the temperature of the glass.

From the two-pulse polarisation echo experiments carried out on HY-1 at two temperatures of $8\,\mathrm{mK}$ and $15\,\mathrm{mK}$, it was found that the echo amplitude was suprisingly small. Comparisons with the echo amplitude of the other multicomponents glasses BK7 and Al-BaSi revealed that the echo amplitude in HY-1 was smaller by two orders of magnitude. Additionally, it was found that the decay rate of the IEAs was also much higher in HY-1 than in the other glasses. The measurement of an echo decay curve in a magnetic field at a temperature of $15\,\mathrm{mK}$ yielded both a higher echo amplitude as well as a smaller decay rate. Thus it was assumed that the small echo amplitude and the fast phase decoherence of the tunnelling systems are partly due to nuclear effects and partly due to an additional decoherence effect most probably caused by the large magnetic moment of holmium. These assumptions can be checked by conducting further two-pulse polarisation echo experiments on the HY-1 glass. For example, measuring echo decay curves in magnetic fields of different strengths and measuring the echo while fixing the pulse separation and varying the magnetic field, as was done in Figure 2.9, could work towards investigating the influence of the magnetic field on the echo amplitude. Additionally, three-pulse polarisation and rotary echo experiments could be conducted on HY-1 in order to investigate the T_1 relaxation mechanism. Plans to produce multicomponent dielectric glasses containing only very small, well-defined amounts of nuclear electric quadrupole moment carrying isotopes are currently underway. By conducting echo experiments on these glasses, it may be possible to shed more light on the matter of nuclear effects in multicomponent glasses.

Bibliography

[And72] P. W. Anderson, B. I. Halperin, C. M. Varma, Anomalous low-temperature thermal properties of glasses and spin glasses, *Philos. Mag.* **25**, 1 (1972)

[Arc13] A. Archer, *Two-pulse dielectric polarisation echo experiments on the aluminoborosilicate glass AlBaSi*, Master Thesis, Heidelberg University (2013)

[Ahr13] F. Ahrens, *Dielektrische Dreipulsechomessungen am Bariumalumosilikatglas AlBaSi*, Bachelor Thesis, Heidelberg University (2013)

[Bar13] M. Bartkowiak, M. Bazrafshan, C. Fischer, A. Fleischmann, C. Enss, Nuclear quadrupole moments as a microscopic probe to study the motion of atomic tunneling systems in amorphous solids, *Phys. Rev. Lett.* **110**, 205502 (2013)

[Baz08] M. Bazrafshan, *Investigation of the microscopic nature of tunneling systems in amorphous glycerol by two-pulse polarisation echo experiments*, PhD Dissertation, Heidelberg University (2008)

[BH77] J. L. Black, B. I. Halperin, Spectral diffusion, phonon echoes, and saturation recovery in glasses at low temperatures, *Phys. Rev. B* **16**(6), 2879 (1977)

[Cla00] J. Classen, T. Burkert, C. Enss, S. Hunklinger, Anomalous frequency dependence of the internal friction of vitreous silica, *Phys. Rev. Lett.* **84**(10), 2176 (2000)

[Ens90] C. Enss, C. Bechinger, M. v. Schickfuß, *Phonons* **89**, Eds: S. Hunklinger, W. Ludwig, G. Weis, World Scientific, Singapore (1990)

[Ens96] C. Enss, R. Weis, S. Ludwig, S. Hunklinger, Coherent echoes in glasses and crystals with point defects, *Czech. J. Phys.* **46**, 3287 (1996)

[Ens05] C. Enss, S. Hunklinger, *Low-Temperature Physics*, Springer-Verlag (2005)

[Esq98] P. Esquinazi, *Tunneling Systems in Amorphous and Crystalline Solids*, Springer Verlag (1998)

[Fey57] R. P. Feynman, F. L. Vernon Jr., R. W. Hellwarth, Geometrical representation of the Schrödinger equation for solving maser problems, *J. Appl. Phys.* **28**(1), 49 (1957)

[Fas10] P. Faßl, *Überprüfung des Modells der spektralen Diffusion mit Hilfe von Polarisationsechomessungen am Borsilikat-Glas BK7*, Bachelor Thesis, Heidelberg University (2010)

[Fic07]   G. Fickenscher, *Einfluss der magnetischen Dipol-Dipol-Wechselwirkung von Kernen auf atomare Tunnelsysteme*, Diploma Thesis, Heidelberg University (2007)

[Fic13]   G. Fickenscher, *Phasenkohärenz und Energierelaxation von Tunnelsystemen in Gläsern*, PhD Dissertation, Heidelberg University (2013)

[Klo08]   F. Klotz, *Untersuchung von Kernquadrupolwechselwirkungen in lithiumdotiertem Kaliumchlorid*, Diploma Thesis, Heidelberg University (2008)

[Glo88]   K. Gloos, P. Smeibidl, C. Kennedy, A. Singsaas, P. Sekowski, R. M. Mueller, F. Pobell, The Bayreuth nuclear demagnetisation refrigerator, *J. Low Temp. Phys.* **73**, 101 (1988)

[Hem]   M. Hempel, PhD Dissertation, Heidelberg University (to be published)

[Hu74]   P. Hu, S. R. Hartmann, Theory of spectral diffusion decay using an uncorrelated-sudden-jump model, *Phys. Rev. B* **9**(1), 1 (1974)

[Hun76]   S. Hunklinger, W. Arnold, Editors: R. N. Thurston, W. P. Mason, *Progress in Physical Acoustics* **12**, Academic Press, New York, 155 (1976)

[Hun77]   S. Hunklinger, *Adv. Solid State Physics* **17**, 1 (1977)

[Hun14]   S. Hunklinger, *Festkörperphysik*, De Gruyter (2014)

[Jae72]   J. Jäckle, On the ultrasonic attenuation in glasses at low temperatures, *Z. Physik* **257**, 212 (1972)

[Jil98]   D. Jiles, *Introduction to magnetism and magnetic materials*, CRC Press, 228 (1998)

[KA62]   J. R. Klauder, P. W. Anderson, Spectral diffusion decay in spin resonance experiments, *Phys. Rev.* **125**(3), 912 (1962)

[Las75]   J. C. Lasjaunias, A. Ravex, M. Vandorpe, S. Hunklinger, The density of low energy states in vitreous silica: specific heat and thermal conductivity down to 25 mK, *Solid State Commun.* **17**, 1045 (1985)

[Luc]   A. Luck, PhD Dissertation, Heidelberg University (to be published)

[Lud02]   S. Ludwig, C. Enss, P. Strehlow, S. Hunklinger, Direct coupling of magnetic fields to tunneling systems in glasses, *Phys. Rev. Lett.* **88**(7), 075501-1 (2002)

[Lud03]   S. Ludwig, P. Nagel, S. Hunklinger, C. Enss, Magnetic field dependent coherent polarisation echoes in glasses, *J. Low Temp. Phys.* **131**, 89 (2003)

[Nag04]   P. Nagel, A. Fleischmann, C. Enss, S. Hunklinger, Novel isotope effects observed in polarization echo experiments in glasses, *Phys. Rev. Lett.* **92**, 24551 (2004)

[Par04]   D. A. Parshin, Oscillations of the electric-dipole echo in glasses in a magnetic field, *J. Low Temp. Phys.* **137**, 233 (2004)

[Phi72]   W. A. Phillips, Tunneling states in amorphous solids, *J. Low Temp. Phys.* **7**, 351 (1972)

[Phi81]   W. A. Phillips, *Topics in Current Physics* **24**, Springer Verlag (1981)

[Poh02]   R. O. Pohl, Liu Xiao, E. Thompson, Low-temperature thermal conductivity and acoustic attenuation in amorphous solids, *Rev. Mod. Phys.* **74**, 991 (2002)

[Pob07]   F. Pobell, *Matter and Methods at Low Temperatures*, 3rd Ed., Springer Verlag (2007)

[Rot13a] D. S. Rothfuß, *Thermische Eigenschaften von supraleitenden massiven metallischen Gläsern bei ultratiefen Temperaturen*, PhD Dissertation, Heidelberg University (2013)

[Rot13b] D. S. Rothfuß, A. Reiser, A. Fleischmann, C. Enss, Noise thermometry at ultra low temperatures, *Appl. Phys. Lett.* **103**, 052605-1 (2013)

[Rue08]   C. Rüdiger, *Polarisationsechomessungen an amorphen Mischungen aus teildeuteriertem und natürlichem Glyzerin*, Diploma Thesis, Heidelberg University (2008)

[Sch12]   C. Schötz, *Dielektrische Dreipuls-Echomessungen und Pausenrotationsechomessungen am Borsilikat-Glas BK7*, Master Thesis, Heidelberg University (2012)

[Sch10]   M. Schwarze, *Überprüfung des Modells der spektralen Diffusion mit Hilfe von Zweipuls-Polarisationsechomessungen an BK7*, Bachelor Thesis, Heidelberg University (2010)

[Str98]   P. Strehlow, C. Enss, S. Hunklinger, Evidence for a phase transition in glasses at very low temperature: a macroscopic quantum state of tunneling systems?, *Phys. Rev. Lett.* **80**(24), 5361 (1998)

[Wei95]   R. Weis, *Messung der dielektrischen Eigenschaften wechselwirkender Tunnelsysteme bei tiefen Temperaturen am Beispiel von KCl:Li*, PhD Dissertation, Heidelberg University (1995)

[Woh01]   M. Wohlfahrt, *Untersuchung der dielektrischen Tieftemperaturanomalien von Mehrkomponentengläsern in Magnetfeldern*, PhD Dissertation, Heidelberg University (2001)

[Wue02]   A. Würger, A. Fleischmann, C. Enss, Dephasing of atomic tunneling by nuclear quadrupoles, *Phys. Rev. Lett.* **89**(23), 237601-1 (2002)

[Wue04] A. Würger, Dephasing of coherent echoes by nuclear quadrupoles, *J. Low Temp. Phys.* **137**, 143 (2004)

[Zac32] W. H. Zachariasen, The Atomic Arrangement in Glasses, *J. Amer. Chem. Soc.*, **54**(10), 3841 (1932)

[Zel71] R. C. Zeller, R. O. Pohl, Thermal conductivity and specific heat of noncrystalline solids, *Phys. Rev. B* **4**, 2029 (1971)

[Zim81] J. Zimmermann, G. Weber, On the excess specific heat of vitreous silica at low temperatures, *Phys. Lett.* **86A**(1), 32 (1981)

Acknowledgements

A big thanks also goes to my girlfriend Isabelle who is always there for me and without whom I would never have become the person I am today.

Ich versichere, dass ich diese Arbeit selbständig verfasst und keine anderen als die angegeben Quellen und Hilfsmittel benutzt habe.

Heidelberg, den 19.12.2014   ....

                                              (Max Hilaire Wolter)